UC Santa Barbara
UC Santa Barbara Electronic Theses and Dissertations

Title

Genesis and Evolution of the Pamir Plateau: a Petrochronologic View

Permalink

https://escholarship.org/uc/item/29j636zf

Author

Stearns, Michael

Publication Date

2014

Supplemental Material

https://escholarship.org/uc/item/29j636zf#supplemental

Peer reviewed|Thesis/dissertation

UNIVERSITY OF CALIFORNIA

Santa Barbara

Genesis and Evolution of the Pamir Plateau: a Petrochronologic View

A dissertation submitted in partial satisfaction of the

requirements for the degree Doctor of Philosophy

in Earth Science

by

Michael A. Stearns

Committee in charge:

Professor Bradley R. Hacker, Chair

Professor John M. Cottle

Professor Phillip B. Gans

September 2014

The dissertation of Michael A. Stearns is approved.

_____
John M. Cottle

_____
Phillip B. Gans

_____
Bradley R. Hacker, Committee Chair

July 2014

Genesis and Evolution of the Pamir plateau: a Petrochronologic View

ACKNOWLEDGEMENTS

VITA OF MICHAEL ANDREW STEARNS
September 2014

EDUCATION
2014   Ph.D. (expected) - Earth Science, UC Santa Barbara
        Dissertation: Genesis and evolution of the Pamir plateau: a petrochronology view
2009   M.S. - Geology and Geophysics, University of Utah
2006   B.S. summa cum laude - Geology and Geography, Eastern Michigan University

PUBLICATIONS

Smit, M., Ratschbacher, L., Kooijman, E., and Stearns, M., in review, Early evolution of the Pamir deep crust from Lu-Hf and U-Pb geochronology, and garnet thermometry: Geology.

Stearns, M.A. and Bartley, J.M., 2014, Multistage emplacement of the McDoogle pluton by magmatic crack-seal, an early phase of the John Muir intrusive suite, Sierra Nevada, California, by magmatic crack-seal growth: Geological Society of America Bulletin, doi: 10.1130/B31062.1.

Stearns, M.A., Hacker, B.R., Ratschbacher, L., Lee, J., Cottle, J.M., and Kylander-Clark, A.R., Widespread, 2013, Synchronous Oligocene-Miocene metamorphism of the deep Pamir and North Himalaya driven by plate-scale dynamics: Geology, vol. 41, p. 1071-1074.

Stübner, K., Ratschbacher, L., Weise, C., Chow, J., Hofmann, J., Khan, J., Rutte, D., Sperner, B., Pfänder, J.A., Hacker, B.R., Dunkl, I., Tichomirowa, M., and Stearns, M.A., 2013, The giant Shakhdara migmatitic gneiss dome, Pamir, India-Asia collision zone: 2. Timing of dome formation: Tectonics, vol. 32, doi:10.1002/tect.20059.

Spencer, K., Hacker, B.R., Kylander-Clark, A.R.C., Andersen, T.B., Cottle, J.M., Stearns, M.A., Poletti, J.E., and Seward, G.G.E., 2012, Campaign-Style Titanite U-Pb Dating by Laser-Ablation ICP: Implications for Crustal Flow, Phase Transformations and Titanite Closure: Chemical Geology, vol. 341, p. 84-101.

Davis, J.W., Coleman, D.S., Gracely, J.T., Gaschnig, R., and Stearns, M., 2011, Magma accumulation rates and thermal histories of plutons of the Sierra Nevada batholith, CA: Contributions to Mineralogy and Petrology, p. 1-17, DOI: 10.1007/s00410-011-0683-7

Schmidt, J., Hacker, B.R., Ratschbacher, L., Stübner, K., Stearns, M., Kylander-Clark, A., Cottle, J.M., Webb, A.A.G., Gehrels, G., and Minaev, V., 2011, Cenozoic Deep Crust in the Pamir: Earth and Planetary Science Letters, vol. 312, p. 411-421.

Stearns, M.A., 2009, Anatomy and assembly of the McDoogle pluton near Sawmill Lake, Central Sierra Nevada, California. [M.S. Thesis] University of Utah, Salt Lake City, UT.

Abstracts:
Rutte, D., Stearns, M.A., Ratschbacher, L., 2014, Shortening and syn-contractional extension: the burial and exhumation history of the Cenozoic Central Pamir Gneiss domes, Tajikistan: EGU General Assembly Abstracts.

Stearns, M.A., Hacker, B.R., Ratschbacher, L., Rutte, D., and Kylander-Clark, A.R., 2013, Two modes of orogenic collapse of the Pamir plateau recorded by titanite: AGU annual meeting.

Stearns, M.A. Hacker, B.R., Kylander-Clark, A.R., Seward, G.G.E., 2013, Fluorine-aided re-equilibration of U-Pb and Zr in titanite: Geological Society of America Abstracts, paper no. 398-11.

Rutte, D., Stearns, M.A., and Ratschbacher, L., 2013, The eastern Central Pamir Gneiss Domes: temporal and spatial geometry of burial and exhumation: EGU General Assembly Conference Abstracts.

Stearns, M.A., Hacker, B.R., Ratschbacher, L., Kylander-Clark, A.R., and Mineav, V., 2012, Early Miocene extension within the Pamir plateau: constructing Temperature-time-Deformation paths with U-Pb titanite geochronology: AGU annual meeting.

Heiner, K.L., Bartley, J.M., Stearns, M.A., and Peterson, E., 2012, Bulk magnetic susceptibility as a proxy for compositional variation in plutonic rocks: Magma mixing can be a problem: Geological Society of America Abstracts, paper no. 92-40.

Stearns, M.A., Hacker, B.R., Kylander-Clark, A.R., Ratschbacher, L., and Seward, G., 2011, Thickening and propagation of the Pamir plateau: insights from monazite and titanite geochronology and trace-element geochemistry, eastern Tajikistan: EOS Trans. AGU, 1(6), Fall Meet. Suppl., abstract #T51J-06.

Hacker, B.R., Ratschbacher, L., Stearns, M.A., McGraw, J., Stubner, K., Kylander-Clark, A.R., Pfander, Jorg, Weise, C., Minaev, V., Gadoev, M., Oimahmadoc, I., 2011, Widespread, synchronous, large-magnitude exhumation of the deep Pamir, Geophysical Research Abstracts, vol. 13, EGU2011-8489

Stearns, M.S., Hacker, B.R., and Kylander-Clark, A.R., 2011, Titanite geochronology from the mid to lower crust of the Pamir plateau, eastern Tajikistan: Journal of Himalayan Earth Sciences, vol. 44, p. 80.

Hacker, B.R., Kylander-Clark, A.R., Lee, J., Cottle, J.M., and Stearns, M.A., 2011, Laser-ablation split-stream petrochronology of Kangmar and Mabja North Himalayan Gneiss Domes: Journal of Himalayan Earth Sciences, vol. 44, p. 25.

Stearns, M.A. and Bartley, J.M., 2009, Coalescence of slipped joints in granitic plutons to form the West Pinnacle Fault, Sierra Nevada, California: Geological Society of America Abstracts, paper no. 173-15.

Stearns, M.A. and Bartley, J.M., 2008, Petrologic controls of the bulk magnetic susceptibility in the McDoogle pluton, Sierra Nevada, California: EOS Trans. AGU, 89(53), Fall Meet. Suppl., Abstract V41D-2138.

Stearns, M.A., Bartley, J.M., and Coleman, D.S., 2008, Rapid emplacement of the McDoogle pluton into the Sawmill Lake shear zone, Sierra Nevada, California: Geological Society of America Abstracts, vol. 40, no. 6, p. 188.

Stearns, M.A. and Bartley, J.M., 2008, Assembly of the incrementally emplaced McDoogle pluton, central Sierra Nevada, CA: Geological Society of America Abstracts, vol. 40, no. 1, p. 92.

Advising faculty:
Bradley R. Hacker - UCSB, Petrology, U/Th-Pb Geochronology, & Plate Tectonics
John M. Cottle - UCSB, Petrology, U/Th-PbGeochronology & Plate Tectonics
Phillip B. Gans - UCSB, Structural Geology, Ar/Ar Geochronology, & Plate Tectonics
Lothar Ratschbacher - TU Freiberg, Structural Geology, Thermochronology, & Plate Tectonics
Jeffrey Lee - CWU, Structural Geology & Plate Tectonics

ABSTRACT

Genesis and Evolution of the Pamir Plateau: a Petrochronologic View

by

Michael Andrew Stearns

The India-Asia collision is the foremost setting to study continent-continent orogenesis, yet mid–deep crustal exposures are rare. In contrast, the Pamir Plateau provides extensive aerial exposure of the deep crust within six gneiss domes. The domes contain a variety of Cenozoic-age metamorphic and igneous rocks exhumed from 8–10 kbar and ≥ 700 ºC. The growth and recrystallization of major and accessory phases in these rocks such as garnet, monazite, and titanite record a robust history of the evolution of the plateau through crustal thickening, metamorphism, and subsequent ongoing collapse. Extracting this record requires accurately understanding and directly linking minerals response to the crustal process of interest. Petrochronology by in situ U/Th-Pb chronometry, trace-element analysis, and thermobarometry is the key to unlocking the physiochemical evolution of the Pamir mid– deep crust, and orogenic processes in general around the world. The following dissertation contains I) an evaluation of whether titanite records volume-diffusion closure or (re)crystallization, II) a comparison of the monazite record from the Central Pamir and Northern Himalaya gneiss domes, and III) campaign-style titanite petrochronology investigation of the onset of collapse in the Pamir plateau.

I. Testing diffusion in titanite using coupled U-Pb and trace-element depth profiles by single-shot laser-ablation split stream (SS-LASS) ICP-MS

Introduction

Core-to-rim elemental and isotopic zoning in minerals has been used to quantify the rates of geologic processes. Much of this work has centered on electron-microprobe analysis (EPMA) of elemental variation, which is typically interpreted using laboratory-determined volume diffusivities (e.g., Cherniak, 1993; Cherniak, 2006). Isotopic zoning in minerals has generally been harder to measure, but major advances have been made with secondary-ion mass spectrometry (SIMS), particularly in the measurement and interpretation of age zoning measured as a depth profile by sputtering from the grain rim inward (e.g., Lee et al., 1997; Grove and Harrison, 1999). The time-consuming nature of SIMS, however, has limited use of this technique. The application of inductively-coupled plasma mass spectrometry (ICP-MS) to depth profiling heralds a new era because of its ability to rapidly measure multiple isotopes and elements simultaneously (e.g., Kohn and Corrie, 2011). One of the biggest advantages to the simultaneous measurement of multiple elements is the ability to use elements with radically different diffusivities as a tool for assessing whether zoning resulted from volume diffusion or other processes.

This paper showcases a new technique, combining the high spatial resolution of single shot (SS)-LA-ICP-MS (Cottle et al., 2009; Cottle et al., 2012) with the high-precision, multi-isotope/element measurement capabilities of laser ablation split stream (LASS; Kylander-Clark et al., 2012) to resolve U-Pb age and trace-element zoning in titanite at the ~100 nm scale. These data are then used to interpret diffusion in and thermal history of titanite. Titanite is an especially useful tool for dating petrologic processes (e.g., Rubatto and

Hermann, 2001; Parrish et al., 2006; Spencer et al., 2013) because it is present in a variety of bulk compositions (Frost et al., 2000), reacts at amphibolite-facies metamorphic conditions (Spear, 1981), contains compositional variation that can be linked to changes in major-phase abundance (Prowatke and Klemme, 2005), and has a calibrated Zr^{4+} thermobarometer (Hayden et al., 2008). Titanite also has experimentally measured Pb and Zr diffusion rates (Cherniak, 2006, etc), but there is some question about the applicability of the experimental diffusion data to natural rocks. The laboratory data predict that Pb and Zr should diffuse at 50 µm length scales in titanite at temperatures of ~600–700 ºC over millions of years (Cherniak06), and yet a number of studies of natural titanite have documented immobility of Pb and Zr at these conditions (Scott and St-Onge, 1995; Zhang and Schärer, 1997; Kohn & Corrie, 2011; Spencer et al., 2013; Stearns et al., 2014). Understanding this discrepancy is important in the use of titanite as a thermochronometer.

Methods

Sample preparation

Titanite from Fish Canyon tuff (FC-1; 28.53 ± 0.05 Ma; Schmitz and Bowring, 2007), Y1710C5 (391.8 ± 2.7 Ma; Spencer et al., 2013), Bear Lake Ridge (BLR; 1047.1 ± 0.4 Ma ; Aleinikoff et al., 2007; Mazdab, 2009), Ontario-2 (ONT-2; 1053.3 ± 3.1 Ma; Spencer et al., 2013), and NIST-610 glass (Gao et al., 2007) were mounted in epoxy and polished to medial sections. Whole titanite crystals from two Pamir rocks, 6907B2 and 999B3, known to have variation in either age or trace-element content were mounted in the same 25-mm diameter epoxy mount such that external crystal faces were exposed at the mount surface without polishing. Titanite 6907B2 has a single-population age of 40.1 ± 0.8 Ma determined using LASS and conventional ICP on many 40 µm-diameter spots from several grains in thin

section (Stearns et al., 2014). Sample 999B3 has not been previously dated, but titanite ages from similar rocks nearby range from ~20–8 Ma (Stearns et al., 2014). No polishing was performed prior to analysis, but mounts were thoroughly cleaned with distilled water prior to analysis.

Analysis

A 193 nm Photon Machines ArF excimer laser equipped with a two-volume Helex® laser cell was used with 0.25 l min^{-1} He total and 1.15 l min^{-1} Ar carrier gas flow per mass spectrometer. The typical washout time following a laser pulse was less than 1 s and 8–10 s of background was collected between laser pulses (Fig. 1). Laser energies of 3 and 5 mJ and a spot diameter of 54 μm were used. The ablated analyte was split and sent to two mass spectrometers: U-Pb isotopic ratios and U, Th, Pb concentrations were measured on a Nu Instruments HR Nu Plasma ICP-MS, and the trace element zirconium (^{90}Zr) was measured on an Agilent 7700S Quadrupole ICP-MS. A complete list of instrument settings is contained in Table 1.

Laser energy was stabilized prior to analysis by firing continuously for several minutes with a blocking shutter in place. Laser spots were placed on the flattest, inclusion-free portion of the grains (Fig. 2). Two cleaning shots were used to remove surface contamination; despite this, some samples show slightly elevated common Pb for the first few analyses. Each depth profile consists of 60 single laser pulses from a 54 μm diameter spot (Fig. 1). The amount of material ablated per laser pulse, or the ablation efficiency, is expected to be constant under such conditions (van Soest et al., 2011), allowing the sampling depth of each laser pulse to

3

be calculated from pit depth. Pit depths were measured using reflected-light microscopy and found to be 4.2 ± 0.1 μm and 8.7 ± 0.1 μm for 100% of 3 mJ

Photon Machines 193nm ArF excimer laser

Cell	Two volume Helex cell (Eggins et al., 1998; Eggins et al., 2005)
Sample transport tubing	0.5-2 m length, Teflon
Washout time	< 1 s
Wavelength	193 nm ArF
Fluence	3 & 5 mJ
Pulse width	< 3 ns @ 1064 nm
Cell volume	3 cm3
Drill depth/pulse	0.1–0.2 um @ 54 um diameter spot (75–100% power)

	Nu Instruments 'HR Nu Plasma' MC-ICPMS	*Agilent 7700X Quadrupole-ICPMS*
Carrier gas flow rate	0.25 l min-1 (He) + 1.15 l min-1 Ar	1.15 l min-1 Ar
Auxiliary gas flow rate	0.8 l min-1 Ar	0.9 l min-1 Ar
Cool gas flow rate	13 l min-1 Ar	15 l min-1 Ar
RF power	1300 W	1350 W
reflected power	<1 W	< 1 W
Sample cone	Ni (1 mm orifice)	Ni (1 mm orifice)
Skimmer cone	Ni (0.7 mm orifice)	Ni (0.7 mm orifice)
Collectors	2 Faraday and 4 electron multipliers	dual-mode electron multiplier
Integration times	200 ms	100 ms
Isotopes measured	204Hg+Pb, 206, 207, 208Pb, 232Th, 238U	90Zr
Reference Materials	Bear Lake titanite (1050 ± XX Ma), Y1710c5 titanite (385.5 ± XX Ma)	Bear Lake titanite (1300 ± 100 ppm Zr), NIST 610 glass (440 ± 16 ppm Zr)

Table 1: Instrument and running parameters for the single shot-laser ablation split stream-inductively coupled plasma-mass spectrometry (SS-LASS-ICP-MS) analysis.
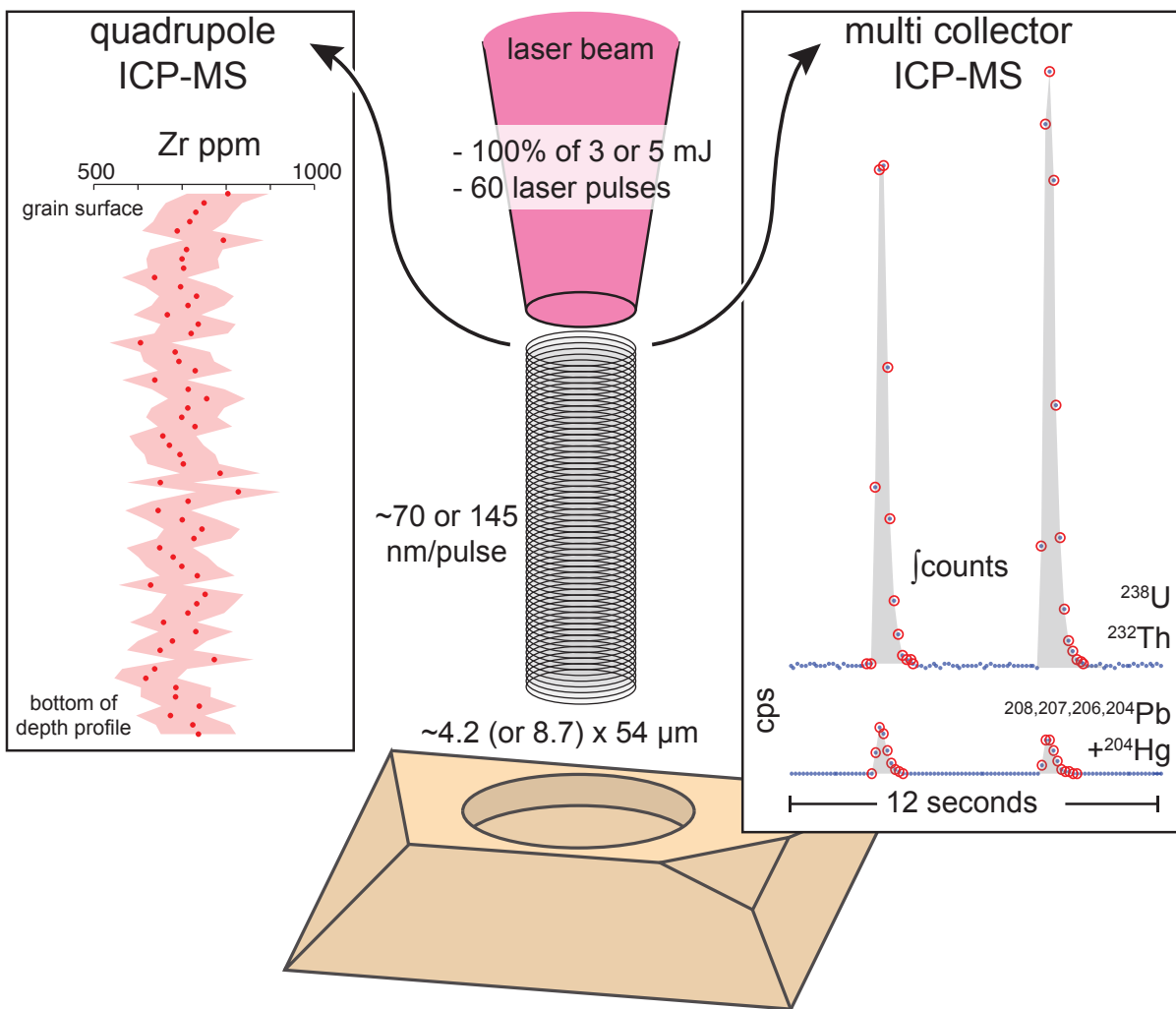
Figure 1: Depth profiling of titanite using the single shot- (SS) laser ablation split stream (LASS) setup consists of a number of single laser pulses that fed into a quadrupole-ICP-MS to measure Zr concentration and a multicollector-ICP-MS to measure U, Th, and Pb isotopic compositions and concentrations. Each SS-LASS datum consists of ~160–330 µm3, 0.6–1.2 ng of titanite, and ~0.03 pg of Pb (50 ppm) compared to traditional analysis of a 40 µm diameter spot fired for 20 s which corresponds to ~12,566 µm3, ~80 ng of titanite, ~5 pg of Pb (50 ppm).
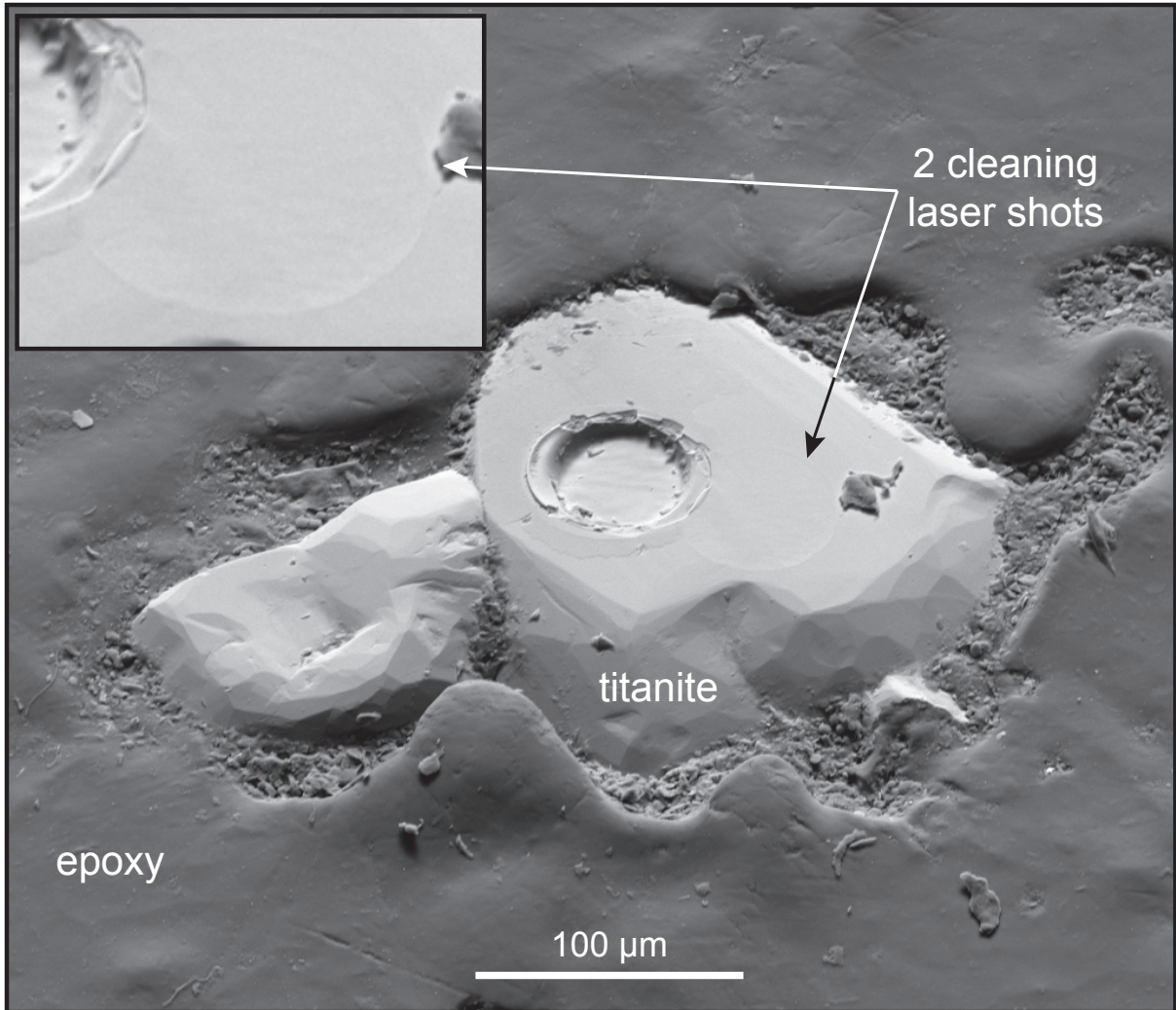
Figure 2: An oblique secondary electron image of an unpolished, titanite grain mount shows the ideal aspect ratio to reduce downhole fractionation and flat pit bottom consistent with homogenous laser ablation. Laser was fired twice prior to analysis (inset) to clean the surfaces of the grains.

and 5 mJ respectively. This is equivalent to ablation rates of ~70 and 145 nm/laser pulse or ~550 and ~1200 pg of titanite per pulse; compare to ~81000 pg of titanite in a traditional 80-shot laser ablation analysis at 3 mJ using a 40 μm diameter spot. For titanite with 50 ppm Pb, an SS-LASS datum contains ~0.03 pg of Pb compared to ~4 pg Pb in a traditional analysis. Signal intensity in homogeneous reference materials typically decreases downhole by ~10–20%.

Data reduction

The raw data were reduced using a MATLAB® program, '*SLaPChron*' (Cottle et al., 2012), modified to process Zr concentrations in addition to the usual U, Th and Pb ratios. Corrections for down-hole elemental and inter-element fractionation, as well as a magnitude correction that adjusts the primary reference material to a known value, were completed in Microsoft Excel®. Time- and depth-dependent elemental and inter-element fractionation were modeled via a linear regression of the primary reference material BLR, and then applied to all unknowns; other regression types (grand mean, polynomial, and exponential) were investigated, and the linear regression gave the best fit. Whereas BLR provides a robust matrix-matched down-hole correction, it is inhomogeneous at the grain scale with respect to U, Th, Pb, and Zr concentrations. The values of BLR were thus measured by EPMA and further calibrated by comparing those measurements to BLR values attained by normalizing to NIST-610 glass (Appendix 1). Due to the different down-hole fractionation of glass, a surface intercept was used when normalizing to NIST-610. This normalization assumes zero elemental fractionation at the beginning of ablation. The robustness of this normalization is confirmed by the observation that the values of BLR obtained in this way are within uncertainty of those measured by EPMA (Table 2).

Sample	Author(s)	method	age (Ma)	± 2sigma (Ma)	concentration (ppm)							
					Zr	± 2σ	Pb	± 2σ	U	± 2σ	Th	± 2σ
Bear Lake Road diggings	Spencer et al. (2013); Mazdab (2009); Aleinikoff et al. (2007)	ICP/EPMA	1047.4	1.4	1470/1300		19.7		300		186	
	this study	EPMA			1485	25	-	-	75–99	20	319–355	13
		SS-ICP	I°	-	1491	157	40	4	134	14	319	34
Ontario-2	Spencer et al. (2013)	TIMS	1053.3	3.1	-	-	19–27	-	77–90		136–198	
	this study	EPMA			1489	25	-	-	48	20	244	13
		SS-ICP	1065	37	1483	148	32	3	106	11	235	24
Y1710C5	Spencer et al. (2013)	TIMS/EPMA	385.8	3.3	128–229							
	this study	EPMA			443	21	-	-	56	20	22	13
		SS-ICP	392	12	426	42	8.7	0.9	111	11	35	4
Fish Canyon titanite (FC-1)	Hayden et al. (2008); Bachmann et al. (2005); Schmitz et al. (2001)	TIMS/EPMA	28.53	0.05	576 & 596; 767	40	1.08–2.22	-	44–69		225–344; 400	
	this study	EPMA			664	23	-	-	-	-	195	13
		SS-ICP	25.8	0.9	699	69	1.4	0.1	41	4	195	19
"Yates Mine" titanite	this study	EPMA	-	-	184	19	-	-	258	20	201	13
		SS-ICP	953	35	197	23	55	4.9	266	34	194	24
6907b2	Stearns et al. (in prep)	EPMA	40.1	0.8	220–675		-		71–283	21	608–735	14
	this study	EPMA			275–366	20	-					
		SS-ICP	42–36	-	128–553	13–56	3.7–5.7	0.4–0.6	104–310	12–33	145–1495	15–180
999b3	this study	EPMA	-	-	238–262	14	-	-	76–100	20	19 & 415–459	14
		SS	18–10.7	-	180–387	20–40	2.2–3.0	0.2	101–276	12–30	28–172	3–18

Table 2: Compilation of age and chemical composition of primary (I°) and secondary (II°) reference materials used in this study.

Uncertainties in isotopic ratios and elemental concentrations were calculated using the population statistics of the primary reference titanite (see Cottle et al., 2012 for a description of error propagation). Each analysis consists of the summed total counts for a single laser pulse, and therefore—in contrast to traditional time-resolved data collection—it is a single datum with no associated external uncertainty. The external uncertainty for individual measurements is computed as the quadratic sum of the counting statistics (internal uncertainty) for the individual analysis plus two standard deviations of the primary reference material mean value for the analytical session. Additional uncertainty is added in quadrature as required to make the secondary reference materials a single population (assuming a Gaussian distribution of uncertainties).

Isotopic ratios were plotted on Tera–Wasserburg concordia diagrams; in this space, mixing between common and radiogenic Pb defines an isochron (Fig. 3). U-Pb ages were [207]Pb-corrected (York, 1968; Compston et al., 1992) using the common-Pb composition defined by the isochron. For data that do not define an isochron, a common-lead composition based on the Stacey and Kramers (1975) model for the approximate age of the sample was used. The upper intercept values are reported in the upper left of the concordia diagrams.

Diffusion modeling

In general, the aim of diffusion modeling is to quantify rates of geologic processes using the movement of elements into or out of a mineral in response to chemical-potential gradients. In this study, we adopt several simplifying assumptions. 1) Diffusion of the elements of interest was driven by a concentration gradient. 2) Diffusion was isotropic. 3) Diffusion can be
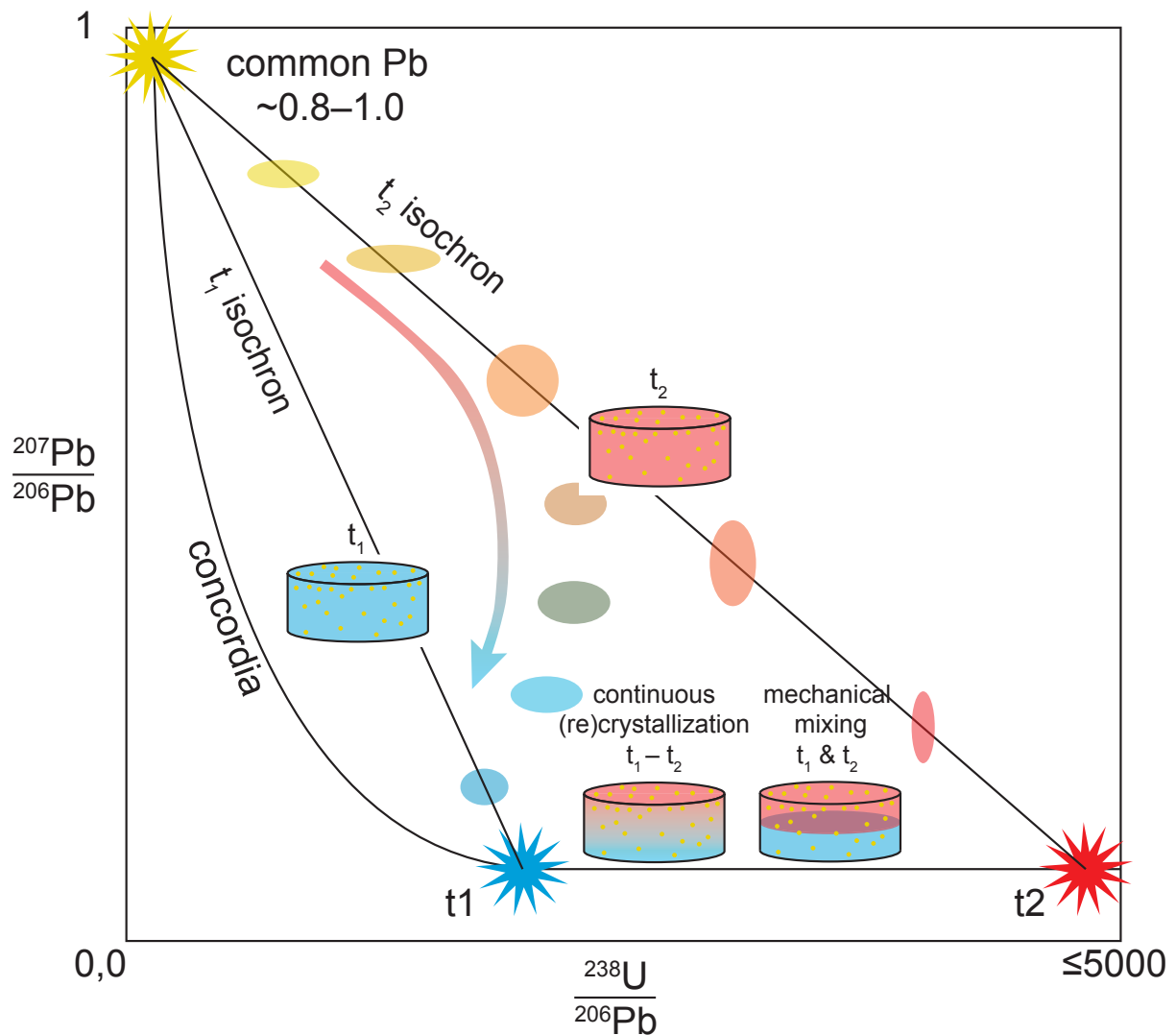
Figure 3: The incorporation of nonradiogenic Pb into titanite necessitates the use of a Tera-Wasserburg concordia plot and calculation of isochron ages. Analyses can be evaluated for mixing among a nonradiogenic Pb composition and one or more radiogenic Pb compositions based on the trajectory of the data down the depth profile.

modeled as a semi-infinite plane source because the titanites in this study are ~100 times larger than the grain radius.

For a semi-infinite plane source and constant diffusivity D (i.e., constant P & T), the normalized concentration profile at time t is given by (Crank, 1975):

$$\left(\frac{C-C_r}{C_c-C_r}\right) = erf\left(\frac{x}{\sqrt{4Dt}}\right) \tag{1}$$

where C is concentration, C_r rim concentration, C_c core concentration, x position, and D diffusivity. (For variable temperature, $\int D(t)dt$ replaces Dt.) The normalized concentration data can be linearized with an inverse error function; the slope m of the inverted data is:

$$m = \frac{1}{\sqrt{4Dt}} \tag{2}$$

This relationship indicates that for a given time and temperature, the slopes of the inverted concentration profiles for different elements differ by $\sqrt{D}$. For titanite, at temperatures of 500–900°C, $D_{Pb} \approx 130\, D_{Zr}$, yielding $m_{Pb} \approx 12\, m_{Zr}$.

Results

Ontario-2

Single-shot dates of Ontario-2 from two analytical sessions (Fig. 4; 1062 ± 30 and 1064 ± 30 Ma) are in agreement with the TIMS age of 1053 ± 3.1 Ma and the LA-ICP-MS age of 1048.7 ± 2.6 Ma (Spencer et al., 2013). Measurements of Zr, Th, and Pb from the same two sessions are within ~10% of the EPMA values (Fig. 6 & Table 2) and in agreement with estimates of the U, Pb, and Th content based on TIMS measurements (Spencer et al., 2013).

The EPMA measurement of U (48 ± 20 ppm) does not agree with the SS-LASS, but is within error of the TIMS measurement—though the latter has large uncertainties (~100%) from estimating the mass of the grains prior to dissolution.

Y1710C5

Single-shot dates of secondary reference titanite Y1710C5 from two analytical sessions (Fig. 4; 392 ± 12 and 400 ± 12 Ma) are within uncertainty of the published TIMS ages (Kylander-Clark et al., 2008; Spencer et al., 2013). Repeat analyses of U, Th, Pb, and Zr in Y1710C5 titanite from the same sessions form a single population. The average Zr concentration of 426 ± 42 ppm is equivalent to the EPMA measurements of the same grain (this study; Table 2), though lower than Spencer et al.'s (2013) EPMA measurement of a different grain. The U content measured by SS-LASS differs from the EPMA measurement by 24%. The Th contents measured by the two techniques agree within uncertainty.

Fish Canyon titanite

Due to low Pb concentrations, SS-LASS dates of the Fish Canyon tuff titanite do not define an isochron. Although little can be learned from the isotopic measurements, the SS-LASS trace-element measurements are in accord with published Zr, U, Th and Pb concentrations (Schmitz and Bowring, 2001; Bachmann et al., 2005; Hayden et al., 2008) and EPMA measurements (Table 2; this study).
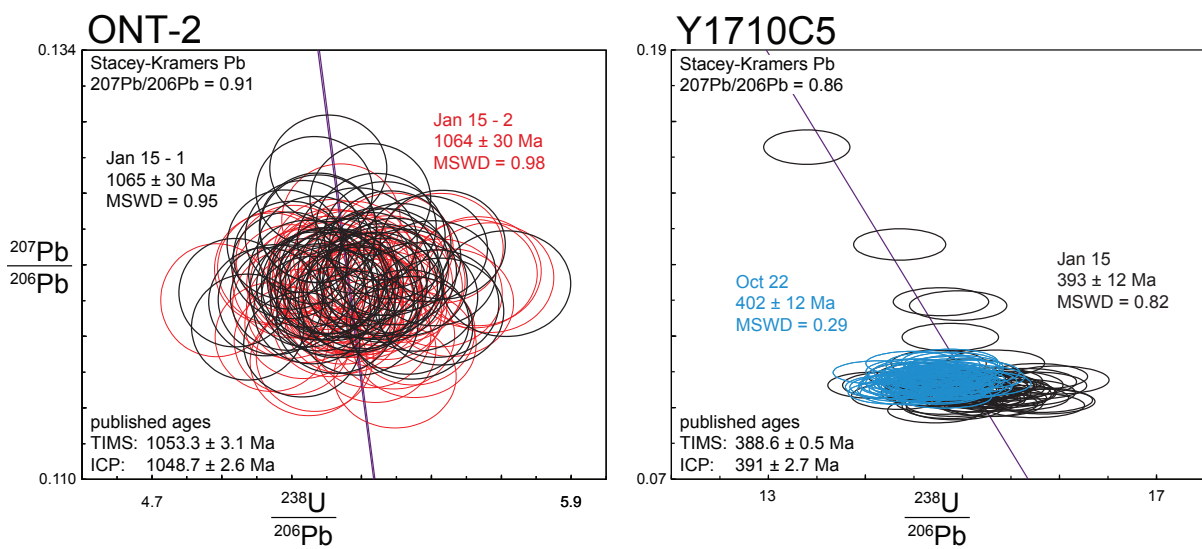
Figure 4: U/Pb data for the secondary reference titanites ONT-2 and Y1710C5 during different analytical runs indicate the ~3% external reproducibility of the U-Pb portion of the SS-LASS method.

Pamir titanite

Both Pamir samples exhibit three-part mixing of common Pb and at least two radiogenic-Pb compositions. The isotopic ratios become more radiogenic and older (lower ^{238}U/^{206}Pb ratio) downhole, toward the center of the grain (Fig. 5).

For sample 999B3, the ^{207}Pb-corrected ages are ~10 Ma near the surface and reach a consistent age of ~18 Ma (~ shot 50) near the bottom of the pit. Analyses of sample 6907B2 are nearly co-linear (Fig. 5B), forming an intercept age; the ^{207}Pb-corrected dates forms a single population. The array has an MSWD = 2.2 and is curved toward lower ^{238}U/^{206}Pb ratios with depth. The upper intercept of the first five shots was used to determine the composition of common Pb; using SK-Pb as the upper intercept increases the ages by ~1.5%. While not statistically robust, the downward age increase is consistent with the trace-element zoning measured in this sample (see next section).

The trace-element concentrations of all elements measured in sample 999B3 increase from rim to core (Fig. 6): Zr from ~200 to 325 ppm, Th from ~40 to 150 ppm, U from ~110 to 250 ppm, and total Pb from ~2.3 to 2.8 ppm. The concentration of Th measured by EPMA was lower than the SS-LASS measurements by ~67%. This inaccuracy likely results from grain-scale heterogeneity within the sample. Each elemental profile has a similar shape: a homogeneous low-concentration rim (first six analyses, or 0–420 nm depth), a transition zone or mantle of increasing concentration (420–700 nm), and a homogeneous inner zone of higher concentration (700–3080 nm). The Zr concentrations correspond to apparent temperatures of 750–800°C for an assumed pressure of 0.8 GPa.
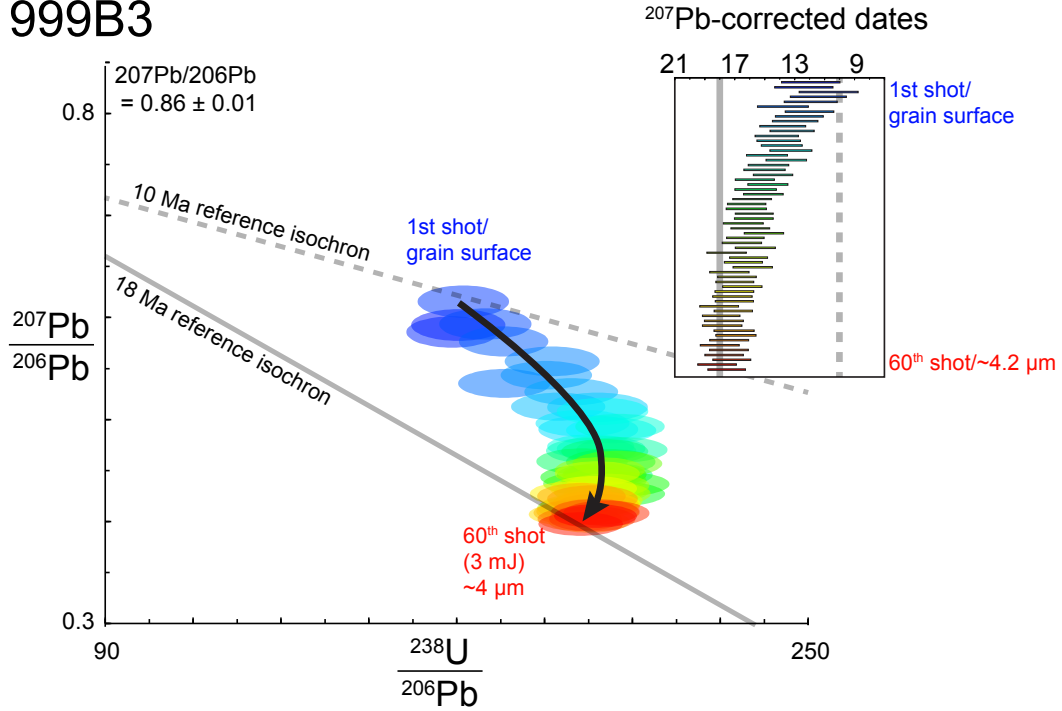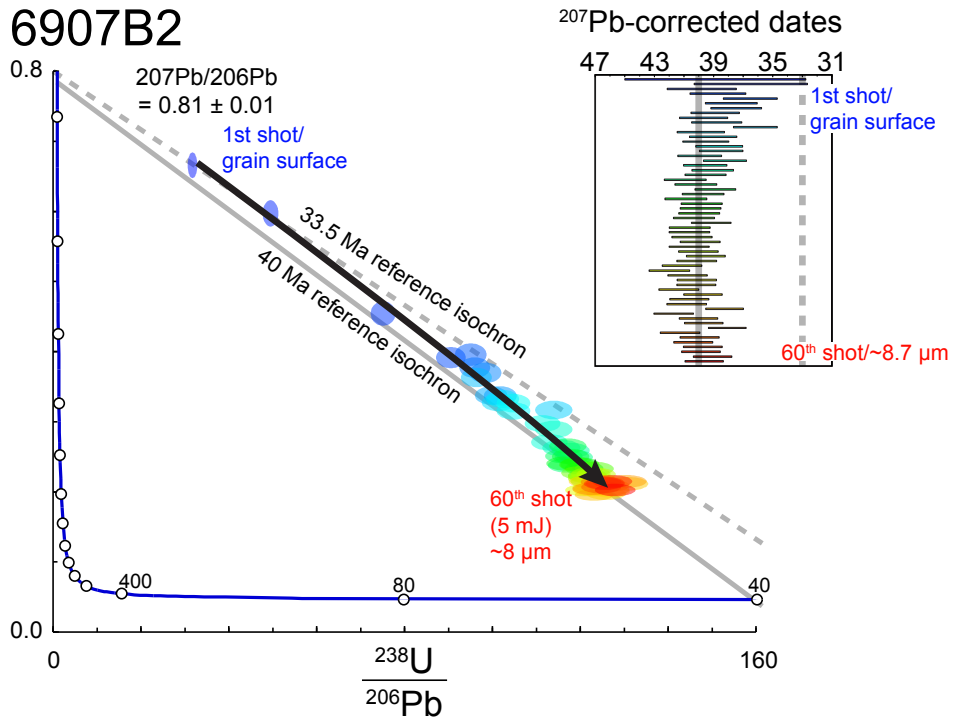
Figure 5: Concordia plot of samples 999B3 and 6907B2 showing age isotopic variation versus depth (contour color). "[207]Pb-corrected" dates (inset) are plotted by depth from crystal face as well. The contour coloring indicates purple as the 1st shot and red the 60th laser shot. Grey lines are reference isochrons to compare the trajectories of the data down the depth profile.
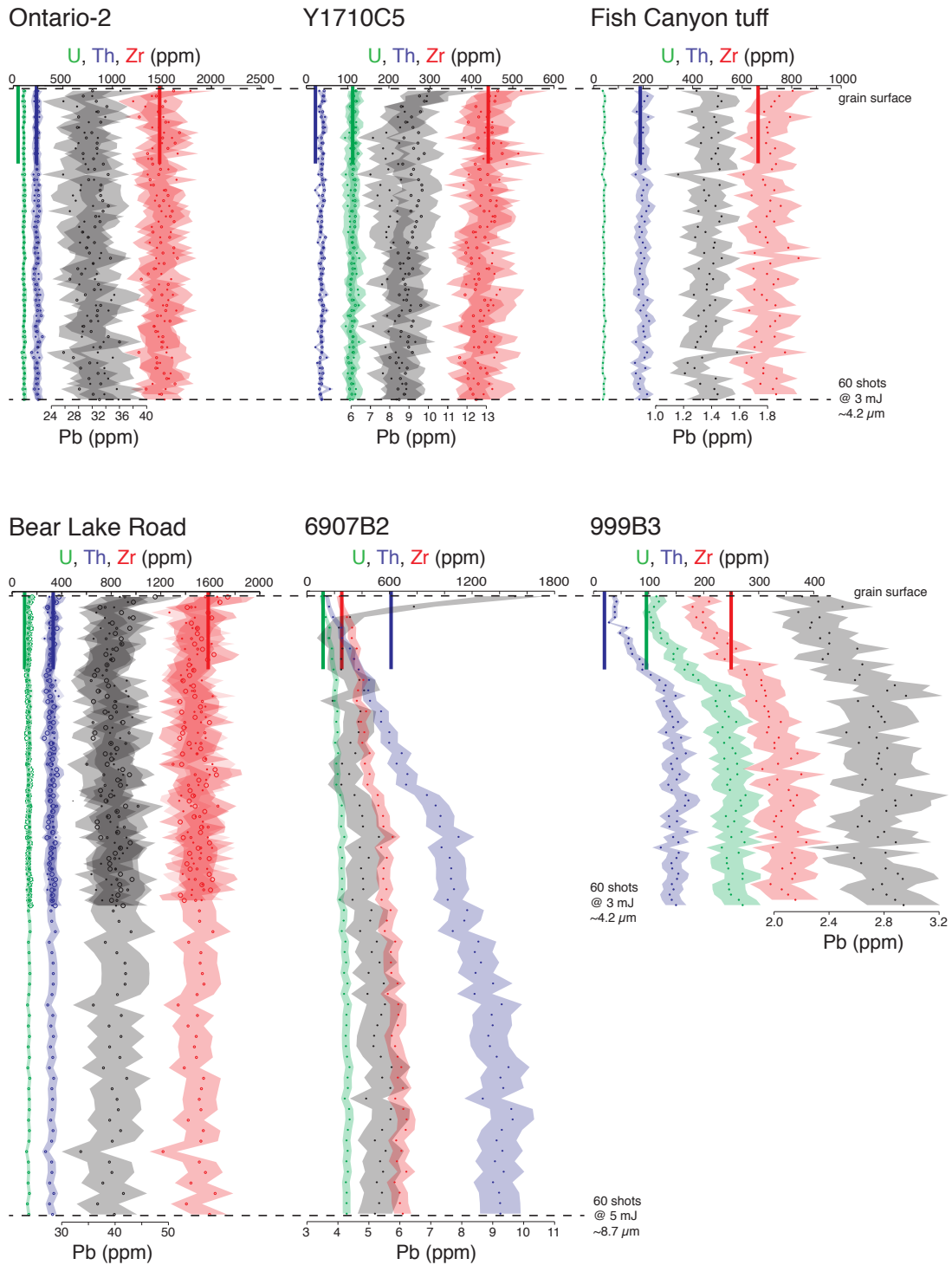
Figure 6: Trace-element contents of the secondary reference materials ONT-2, Y1710C5, Fish Canyon titanite, and unknown samples 6907B2 and 999B3, as a function of depth. Solid lines are mean EPMA analyses and extend to 1 µm depth to show likely interaction volume of the electron beam. Error envelope is 2 standard deviations uncertainty.

The trace-element concentrations of all elements measured in sample 6907B2 increase from rim to core (Fig. 6): Zr from ~125 to 550 ppm, Th from ~150 to 1500 ppm, U from ~105 to 310 ppm, and total Pb from ~3.7 to 5.7 ppm. Each elemental profile has a similar shape: low concentration rim that increases rapidly toward a homogeneous core. The Zr concentrations correspond to apparent temperatures of 770–830°C for an assumed pressure of 0.8 GPa.

Discussion

Interpretation of the Elemental Gradients

If the measured concentration gradients are the result of volume diffusion, each element gradient should define a unique $\sqrt{4Dt}$ slope that scales with the element diffusivity. In particular, as noted above for titanite, $m_{Pb} \approx 12\ m_{Zr}$. Figure 7 illustrates that when the concentration gradients are inverted through erf^{-1}, all of the elements define the same $\sqrt{4Dt}$ slope. The measured concentration gradients cannot, therefore, be the result of volume diffusion; process(es) other than volume diffusion must have been responsible. Kohn and Corrie (2011) came to a similar conclusion for Zr and Pb in Himalayan titanite.

Many studies using zoning of a single element to quantify rates of geologic processes. Although the concentration gradient of a single element can be fitted to a diffusion model and a thermal history can be calculated, one of the strengths of multi-element depth profiling lies in the ability to assess whether the concentration gradients of elements with different
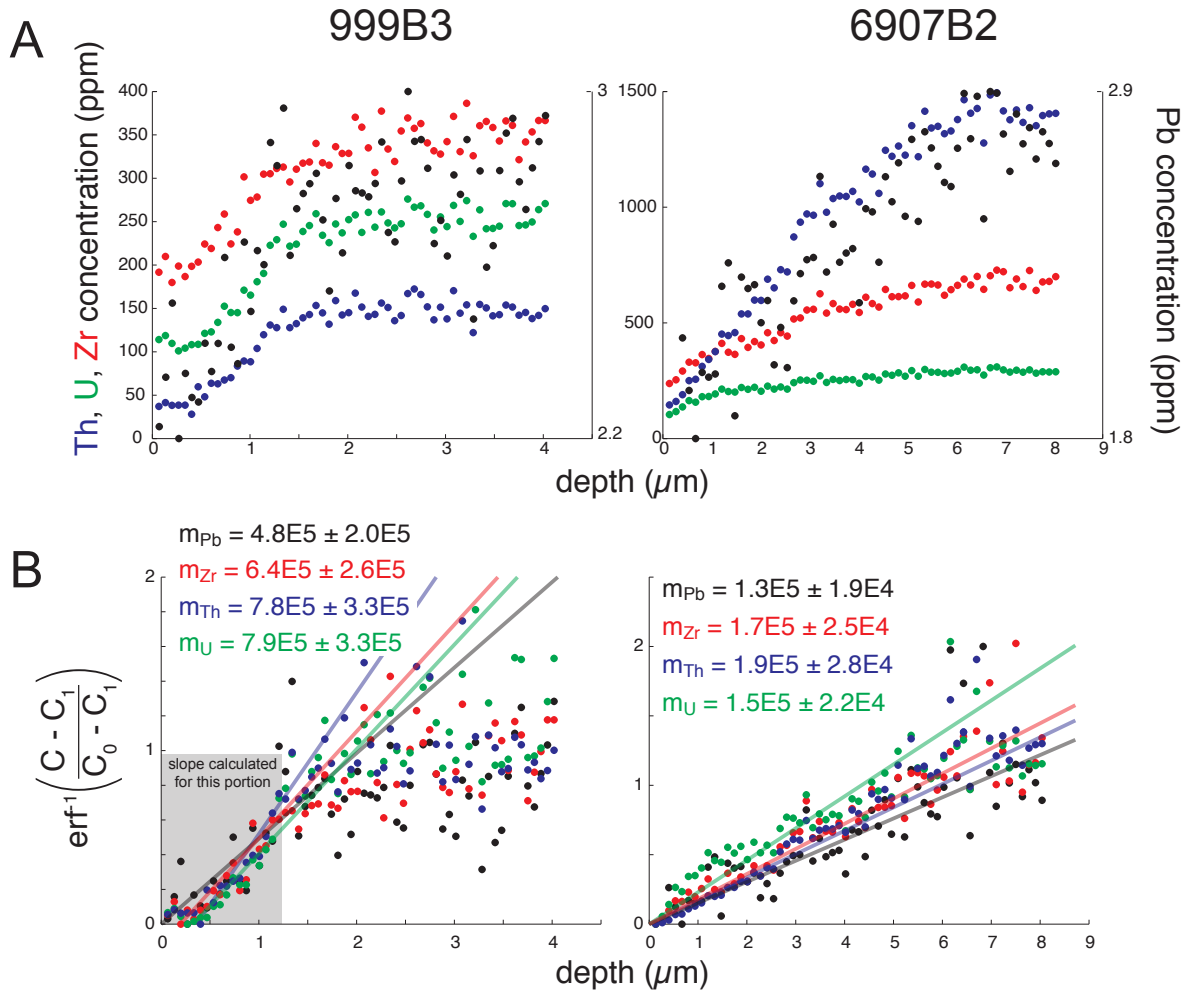
Figure 7: A) Concentration profiles and B) inverted profiles for samples 999B3 and 6907B2. The slope of the inversion (eqn. 2), proportional to D and t, can be compared to Pb, which is the fastest diffusing element measured. The slope of each element within each sample are identical within error.

diffusivities lead to the same inferred thermal history. The data presented here show that using a single element to model thermal history is tenuous because of the non-uniqueness of the error function solution to the diffusion equation. For example, interpreting the data for titanite 6907B2 as the result of volume diffusion leads to timescale at 750°C of ~300 yr for Pb and~30 kyr for Zr.

If the measured elemental concentration gradients are not the result of volume diffusion, they may instead be the result of growth zoning and reflect time-dependent changes in partitioning of Th, U, Pb and Zr into titanite. If so—and if not modified by diffusion or another process—cooling rates can be extracted from the zoning by combining U-Pb ages and Zr apparent temperatures (Fig. 8). Cooling rates calculated from linear regression of the data are ~6 ± 1 ºC/Myr from ~18–11 Ma for 999B3, and ~20 ± 5 ºC/Myr from ~41–37 Ma for 6907B2. These cooling rates are geologically reasonable given existing [40]Ar/[39]Ar, fission track, and U-Th/He thermochronology (Rutte et al., 2013; Stübner et al., 2013b). Multi-mineral cooling ages from near sample 999B3 indicate a faster, ~70 ± 16 ºC/Myr, cooling rate from ~8 to ~2 Ma of (Stübner et al., 2013b).

Conclusions

Single shot-LASS depth profiling is capable of accurately and precisely (~5–10%) determining the U-Pb age and trace-element concentrations in titanite. The near-rim trace-element zoning in titanite can be modeled using a simple semi-infinite half-space diffusion model. Measuring multiple trace elements with different diffusivities is necessary for interpreting a mineral thermal history. Pamir titanite that experienced amphibolite facies metamorphism apparently did not experience significant volume diffusion modification

following (re)crystallization. Detailed temperature-time histories can be extracted by the concurrent measurement of U-Pb dates and Zr^{+4} apparent temperatures.
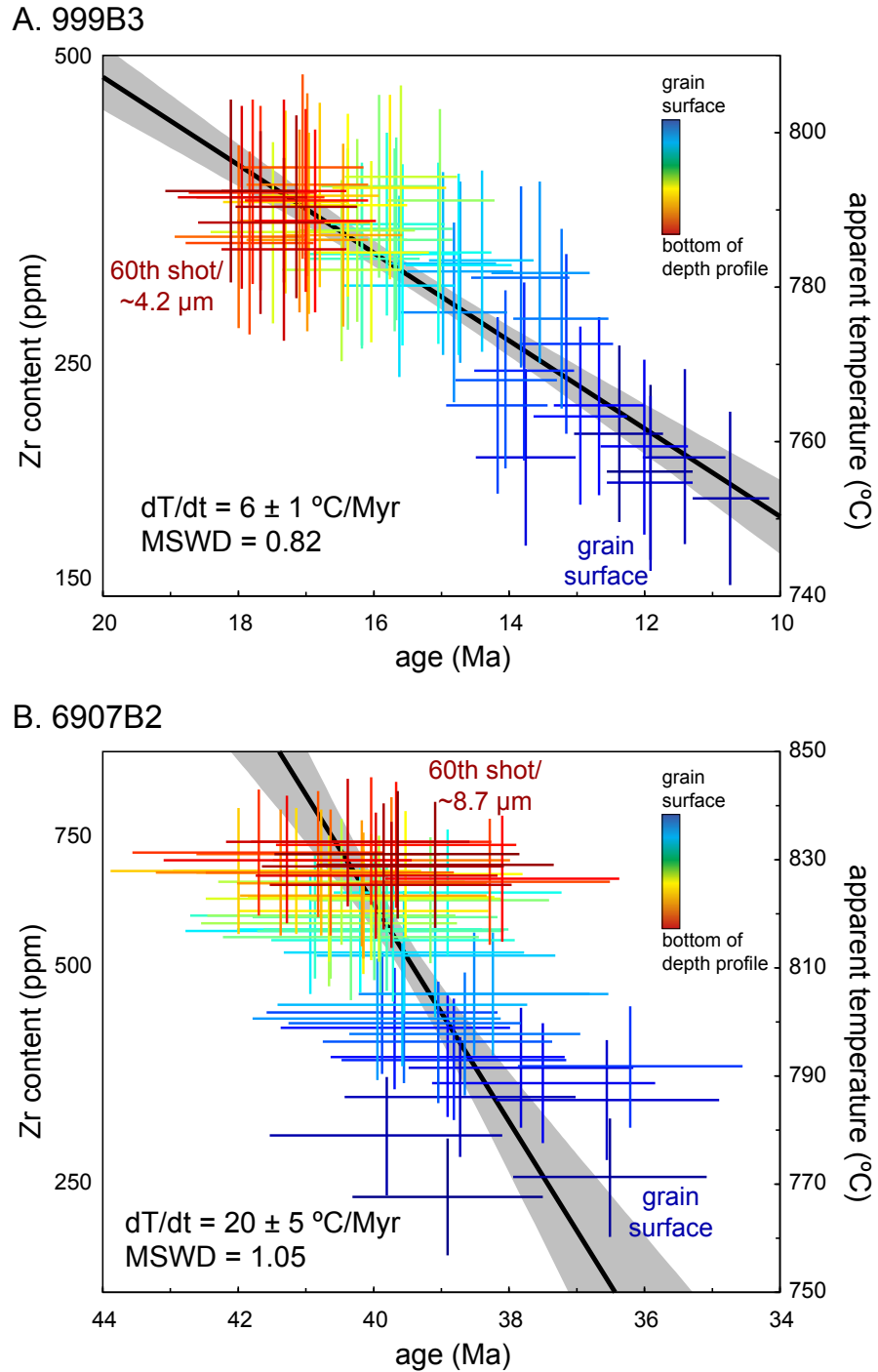
Figure 8: Cooling trajectories can be calculated from the apparent Zr temperatures (Hayden et al., 2008) and U-Pb age data. Linear regression of the data yield cooling rates of 6 ± 1 and 20 ± 5 ºC/Myr for 999B3 and 6907B2 respectively. The cooling rate for 999B3 from ~19–10 Ma, are slower than thermochronometrically determined rates of ~70 ºC/Myr (for ~8–2 Ma) for the same area.

II. Synchronous Oligocene–Miocene metamorphism of the Pamir and North Himalaya driven by plate-scale dynamics

Introduction

Tectonism in orogens can be driven by local differences (e.g., climate, rheology, rock type, crustal heterogeneities) or external boundary conditions (e.g., plate velocity). For example, changes in density distributions or thickness may give rise to buoyancy or gravitational potential energy (GPE), body forces that may drive ductile flow if they exceed rock strength. Changes in boundary forces may be linked to specific tectonic events, including crustal thickening, convective removal of lithosphere, or changes in plate dynamics (Forsyth and Uyeda, 1975).

Crustal thickening, foundering, and slab breakoff are widely invoked end-member processes occurring in orogens. Crustal thickening both directly increases and modifies GPE via phase changes. Thickening of radiogenic crust also causes temperature to increase over $\sim 10^7$ Myr (England and Thompson, 1984), causing thermal weakening and potentially enabling flow (England and Houseman, 1989). Foundering of a gravitationally unstable portion of the lithosphere can change GPE dramatically and lead to conductive or advective heat transfer into the crust. Slab breakoff may lead to comparable changes in the upper plate as well as change trench suction, colliding resistance, or slab resistance.

The India–Asia collision (Fig. 9) affords an opportunity to examine the interplay between far-field and local causes of thickening and exhumation by examining the middle to lower crustal chemical evolution of the orogen through time and space. Here we present new monazite petrochronology (Kylander-Clark et al., 2012 and references therein) that
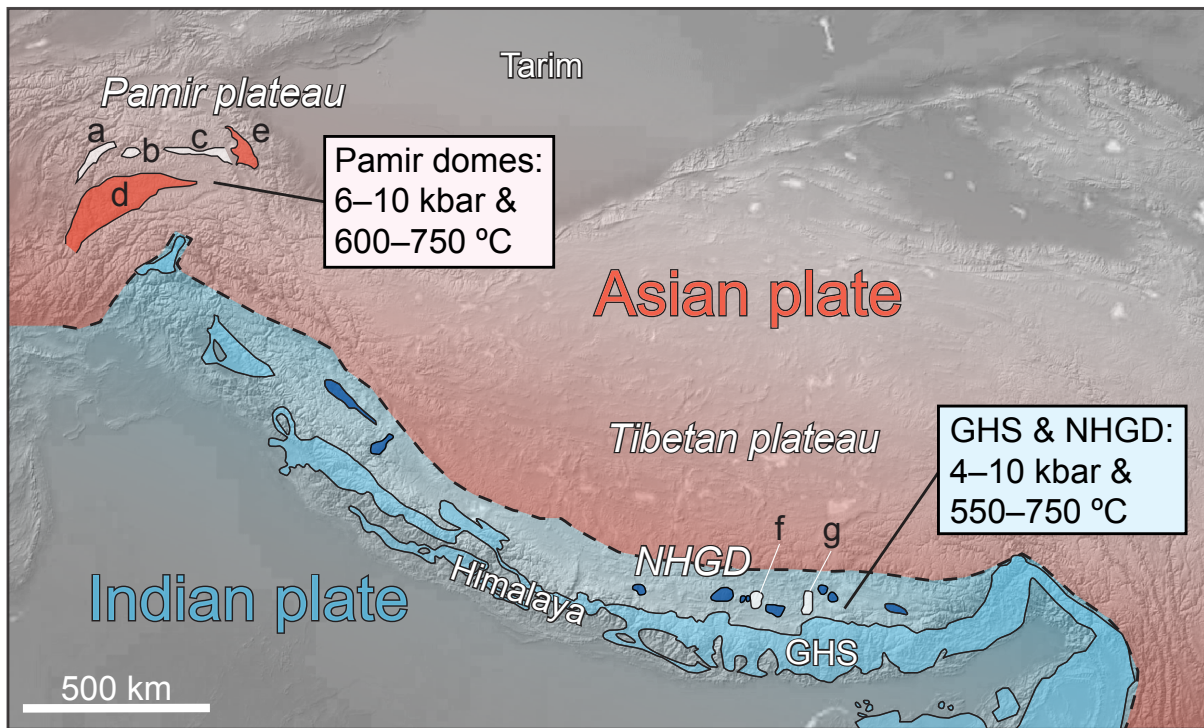
Figure 9: Geologic-topographic map, highlighting locations of north Himalayan and Pamir gneiss domes within the Cenozoic India-Asia orogen. North Himalayan gneiss domes are part of the Indian plate (blue) south of Indus-Yarlung suture, and Pamir domes formed within the Asian plate (red). Domes (those discussed in this paper are shown in white): a—Yazgulom; b—Sarez; c—Muzkol-Shatput; d—Shakhdara; e—Muztagh Ata–Kongur Shan; f—Mabja; g—Kang- mar. Pressure-temperature determinations for the Pamir and the Hi- malaya: Greater Himalayan Series (GHS) (e.g., Simpson et al., 2000), northern Himala- yan gneiss domes (NHGD) (Lee et al., 2000, 2004), and Pamir (Grew et al., 1994; Schmidt et al., 2011).

demonstrates that the burial and exhumation of widely separated—and apparently unrelated—crustal sections in the Pamir and north Himalaya were synchronous, and thus best ascribed to plate-scale forces rather than local processes.

Geologic Setting

The Himalayan front includes two arcuate belts of high-grade metamorphic and igneous rocks: the Greater Himalayan Series (GHS) and the northern Himalayan gneiss domes (NHGD; Fig. 9). These two belts contain underthrust Indian plate schist, marble, paragneiss and orthogneiss exhumed in the late Cenozoic (Lee and Whitehouse, 2007). Pressure–temperature–time (*P-T-t*) data indicate Barrovian metamorphism from ~40 Ma until 16 Ma, with crustal melting from 24 to 12 Ma (Cottle et al., 2009). Nelson et al. (1996) and others proposed that the GHS and NHGD were metamorphosed while being thrust beneath the Tibetan Plateau. The GHS was later extruded by mid-crustal flow in response to a N–S gradient in GPE, while the NHGD were exhumed by a combination of diapiric rise, transport over a thrust ramp, and upper-plate extension (e.g., Quigley et al., 2006).

In the Pamir, Barrovian metamorphic rocks and associated igneous rocks also crop out in a series of domes that were exhumed by N-S extension. Like the NHGD, the Pamir domes are built of paragneiss, schist, orthogneiss and marble and intruded by calk-alkaline igneous rock (Schwab et al., 2004). In contrast, the domes of the Pamir crop out within the orogen interior far north of the Indus–Yarlung suture and represent crust of the Asian plate (Schwab et al., 2004). These Barrovian metamorphic rocks also experienced metamorphic conditions typical of the mid–lower crust (Fig. 9).

Thus, the eastern segment of the orogen exposes two arcuate belts of Cenozoic Indian plate-derived metamorphic rocks along the southern limit of the orogen whereas the western segment of the orogen has Cenozoic, Asian plate-derived metamorphic domes in its interior (Fig. 9). Here we present new monazite petrochronology (Fig. 10) for the NHGD and Pamir domes to show, in spite of these profound differences, that rocks within these domes experienced peak metamorphic conditions synchronously. This finding suggests that the driving force(s) for these events were not different, local phenomenon specific to the Himalaya and the Pamir, but plate-scale dynamics capable of driving synchronous response of the entire the India–Asia collision.

Monazite Geochronology by LASS

Monazite is an ideal phase for dating the P–T–t–deformation paths of metapelitic rocks because it readily reacts with major phases such as garnet, enabling one to link dates to *P,T*-dependent metamorphic reactions (e.g., Foster et al., 2000). Monazite formed at different times may have distinct chemical zones reflecting growth or recrystallization in the presence or absence of other phases (Williams et al., 1999). For example, heavy rare earth-elements (HREE) and yttrium (Y) strongly partition into garnet (or xenotime), potentially enabling the use of HREE concentrations in monazite to monitor the participation of those minerals in monazite-forming reactions (Hermann and Rubatto, 2003); below we report Yb/Gd ratios as a metric of HREE depletion or enrichment.

Recent advances in LA-ICP-MS allow more robust interpretation of dates using chemical information collected simultaneously with isotopic age data (Kylander-Clark et al., 2012). Laser ablation split-stream ICP-MS (LASS) enables determination of in situ U/Th-Pb dates
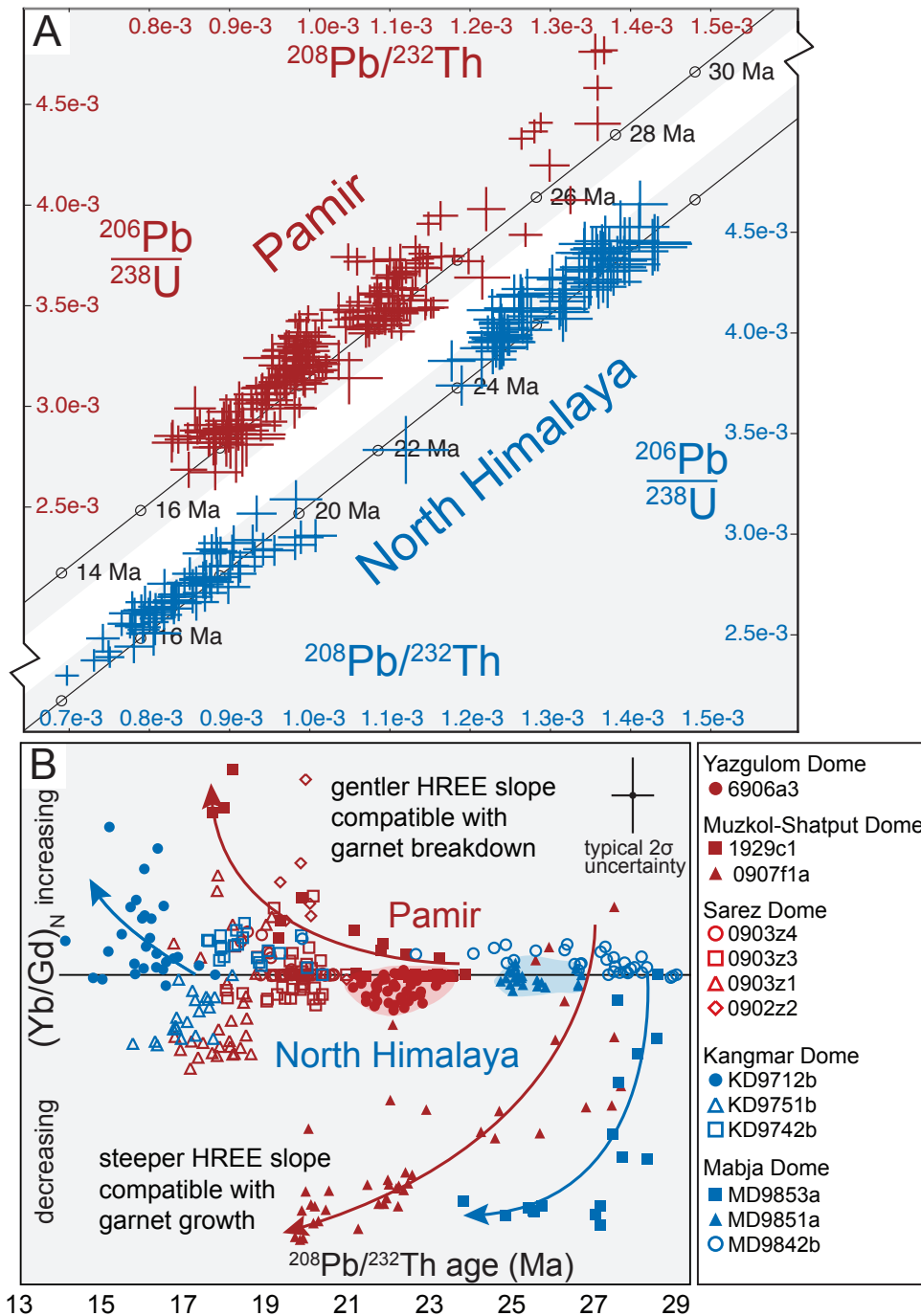
Figure 10: A) U/Th-Pb monazite dates from Pamir (red) and north Hima-layan (blue) gneiss domes show similar periods of monazite (re)crys-tallization at ca. 28–17 Ma and ca. 29–14 Ma, respectively. B) Normal-ized Yb/Gd ratio versus 208Pb/232Th age. Mean Yb/Gd ratio of the five oldest spots per sample are normalized to zero to track enrichment or depletion through time. Most samples have invariant heavy rare earth element (HREE) slope. HREEs decrease over time (downward arrows) in older monazite in two samples, compatible with garnet growth. HREEs increase over time (upward arrows) in younger monazites in two other samples, compatible with garnet breakdown.

and REE abundances from the same ablated material sent simultaneously to a multi-collector ICP-MS (for U/Th-Pb isotopes) and a single-collector ICP-MS (for REE).

We used LASS to measure U/Th-Pb dates (Fig. 10A) and REE concentrations (Fig. 10B; suppl. data) in monazite from seven samples from three Pamir domes and six samples from two NHGD (Fig. 9). All the samples are pelitic to semipelitic gt + bt ± st ± ky ± sil schists. Garnet in these samples typically have prograde zoning and are partially resorbed; a minority are neither zoned nor resorbed. Pseudosections indicate that garnet growth in these rocks was driven partly by increasing temperature but primarily by increasing pressure (e.g., Schmidt et al., 2011). Textures indicate that monazite in most samples was produced by reaction between biotite and apatite (Bingen et al., 1996); monazite associated with staurolite may have been generated by breakdown of gt + chl + ms (Kohn and Malloy, 2004). Monazite grains exhibit several types of zoning patterns (Fig. 11; Appendix 2); most have partially recrystallized, subhedral to anhedral low-Y cores overgrown by high-Y rims, but a minority have oscillatory zoning or are homogeneous. Different compositional zones were targeted for dating and boundaries were avoided by careful laser spot (7–10 μm) placement (Fig. 11; Appendix 2).

The NHGD monazite dates indicate nearly continuous (re)crystallization from 29 to 14 Ma (Fig. 10A and 10B; blue data). Monazite in two Mabja dome samples shows no change in Yb/Gd from 29 to 19 Ma, whereas monazite in a third sample shows increasing depletion (decreasing Yb/Gd) from 29–24 Ma. Some older Mabja monazite are included in garnet, kyanite, or staurolite, whereas most of the younger dates (<20 Ma) are from matrix grains. Monazite in three Kangmar dome samples ranges from 20 to 14 Ma. Two Kangmar samples
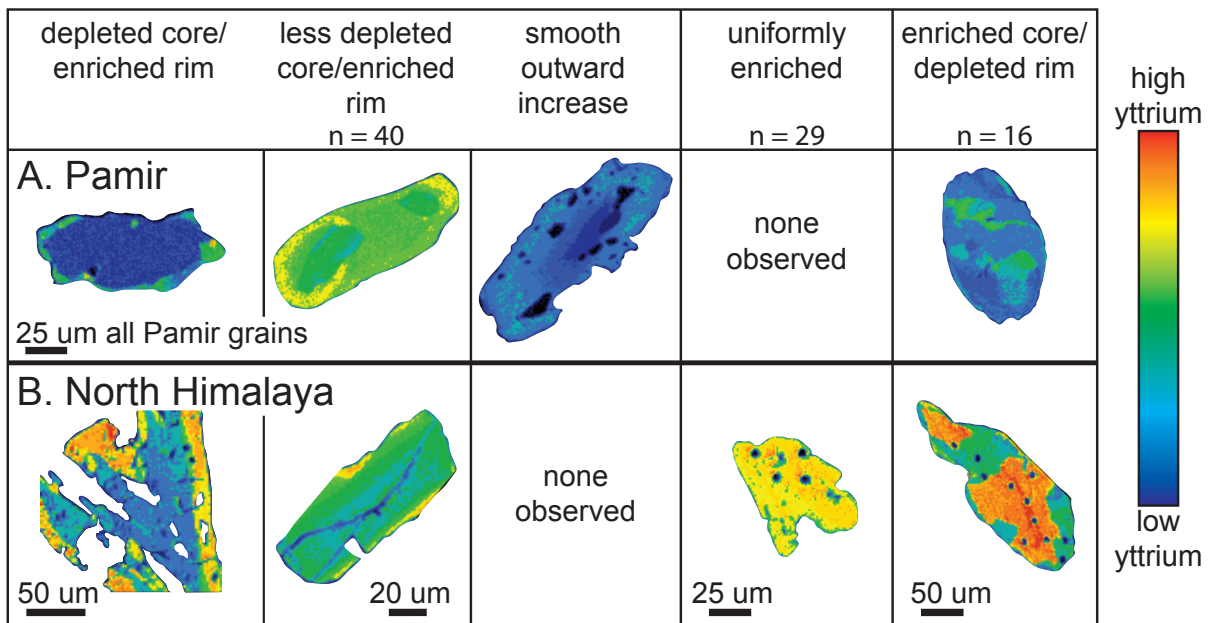
depleted core/ enriched rim	less depleted core/enriched rim n = 40	smooth outward increase	uniformly enriched n = 29	enriched core/ depleted rim n = 16
A. Pamir			none observed	
25 um all Pamir grains				
B. North Himalaya		none observed		
50 um	20 um		25 um	50 um

high yttrium — low yttrium

Figure 11: X-ray maps of characteristic monazites from Pamir (A) and north Himalayan (B) domes. Grains with yttrium (Y)-depleted cores and Y-enriched rims are most abundant (n = 40); oscillatory zoning or embayed cores/irregular zoning textures are less common. Y is simi- lar in ionic radius to Ho, a heavy rare earth element (HREE) (Shannon, 1976), such that these Y maps are a proxy for HREE maps. Spots in some grains are laser holes. Total number of grains mapped is n = 85.

exhibit no change in Yb/Gd over time, where a third sample became progressively enriched in HREE (increasing Yb/Gd).

Monazite dates from the Pamir domes indicate growth or recrystallization from 28 to 18 Ma (Fig. 10A and 10B; red data). No sample spans the entire age range, rather each shows a limited episode of (re)crystallization. Yazgulom dome monazite ranges from 23 to 21 Ma and have constant Yb/Gd. Monazite from the Sarez dome ranging from 21 to 17 Ma has variable Yb/Gd with no coherent pattern. Monazite in the Muzkol–Shatput dome has dates of 28–18 Ma; monazite in one sample became more depleted (decreasing Yb/Gd) from 28 to 19 Ma whereas another sample became more enriched (increasing Yb/Gd) from 24 to 17 Ma. In summary, although most Pamir monazite have invariant Yb/Gd values, samples that exhibit variation have older monazite that became more depleted and younger monazite that became progressively more enriched (Fig. 10B).

Discussion

Monazite U/Th-Pb dates from the Pamir and NHGD span a nearly identical range: 28–16 Ma in the Pamir and 29–14 Ma in the NHGD (Fig. 10). Moreover, the age-related changes in monazite composition (Fig. 10B) are consistent with synchronous peak metamorphism. Older monazite in the Pamir became progressively HREE depleted from 28 to 19 Ma, and NHGD monazite (re)crystallized at this same time followed the same trend. Pamir monazite younger than 23 Ma became enriched in HREE, and NHGD monazite behaved similarly.

We interpret monazite that is HREE + Y depleted, and included within peak assemblage minerals, to record prograde metamorphism in the presence of garnet and/or xenotime (e.g., à

la Foster et al., 2004). Some elemental zoning within monazite does not correlate with age, perhaps due to the relative immobility of REE relative to Pb (Cherniak et al., 2004). HREE depletion in monazite is compatible with increasing garnet mode (which, as noted above, is primarily a function of pressure in these pelites)—or Rayleigh fractionation by phases that partition HREE—but in any case incompatible with garnet breakdown. We interpret matrix monazite that is HREE + Y enriched to record the breakdown of garnet. HREE-enriched monazite could have crystallized from a melt, but the absence of melt textures in the Central Pamir domes supports a decompression and/or cooling interpretation. This long-term pattern of monazite (re)crystallization—early HREE depletion of grains followed by younger HREE enrichment of grains—is most simply interpreted as the result of garnet growth followed by garnet breakdown. The tectonic implication is that crustal thickening produced the heating necessary for garnet growth and exhumation enabled cooling and/or decompression that drove garnet decomposition.

The matching ~28–15 Ma records of monazite (re)crystallization in the Pamir and Himalayan domes is surprising in light of the disparate locations and genesis of the domes: to recap, the NHGD are once-buried Indian crust at the southern margin of the orogen; the Pamir domes are exhumed Asian crust in the center of the orogen. These new data suggest an orogen-scale process that simultaneously buried and partially exhumed both Indian and Asian crust along the margin and core of the orogen.

Synchronous Pamir and Himalaya Tectonism Driven by Plate Tectonics
The synchronous monazite (re)crystallization histories of the Pamir and Himalaya deep crust are most easily explained as the result of changes in large-scale plate dynamics[1]. Local

changes in stress state, rheology, or GPE in the Pamir and Himalaya could only have produced synchronous changes by coincidence. Following the initial subduction of Indian continental crust at ~50 Ma (e.g., van Hinsbergen et al., 2011), the subducted Indian slab is inferred to have broken off based on tomographic images beneath both the Pamir (Negredo et al., 2007) and Tibet (Replumaz et al., 2010), and on changes in the style and location of volcanism in Tibet (Kohn and Parkinson, 2002; Chung et al., 2003, 2005). At ~35 ± 5 Ma, subduction of India is inferred to have recommenced, with a buoyant lower plate forcing the upper plate to contract (Chung et al., 2003; Replumaz et al., 2010). We propose that this thickening is reflected in the ~28 Ma initiation of garnet-present monazite (re)crystallization in the Pamir and in the Himalaya. Monazite and zircon dates, as old as ~39 Ma, have been documented in the GHS and NHGD (Lee and Whitehouse, 2007; Cottle et al., 2009; Streule et al., 2010). Regional Barrovian metamorphism likely began at least by this time and possibly persisted for ~20 Myr. Our monazite data suggest that orogen-scale thickening then continued until ca. 20 Ma when a second major event initiated or permitted exhumation.

It seems unlikely that the NHGD and Pamir fortuitously thickened in such a way that internal heating alone precipitated simultaneous extension. Similarly, it seems improbable that the Himalaya and the Pamir—quite different in their GPE gradients today—both reached GPE gradients conducive to N–S extension at the same time. More plausible is that the Pamir and Himalaya were both undergoing thickening before 28 Ma and that both reached a sufficiently high GPE and a weak mid–lower crust by 20 Ma that a change in a system-wide boundary condition was able to trigger extension. That change might have been the second slab tearing event that has been postulated—on the basis of tomography and magmatism—to have begun at ~25–20 Ma (Replumaz et al., 2010; DeCelles et al., 2011). We propose the monazite dates

32

may reflect this switch, with the youngest HREE-depleted (i.e., prograde or peak metamorphic), 23–20 Ma monazite in both the Pamir and Himalaya tracking slab tear-off and the initiation of N–S extension.

Conclusions

Monazite dates record protracted high-grade metamorphism from ~28–15 Ma in both the north Himalayan gneiss domes and the Pamir gneiss domes. Middle- to lower-crustal rocks in significantly different parts of the orogen experienced at least 8 Myr of burial beginning by at least ~28 Ma, transitioned to exhumation by N–S crustal extension at the same time, ~20 Ma, and saw the end of monazite recrystallization at ~15 Ma. The beginning and end of Barrovian metamorphism in the Pamir and Himalayan domes relative to other significant tectonic events such as the collision of India and the transition to intra-plateau extension suggests a common orogen-wide change in plate dynamics drove the evolution of these spatially distinct gneiss domes. This orogen-scale perspective—linking the synchronous evolution of the Pamir and north Himalayan Gneiss domes implies local processes were subordinate to larger, plate-scale processes.

III. Titanite petrochronology of the Pamir gneiss domes: Implications for mid–deep crust exhumation and titanite closure to Pb and Zr diffusion

Introduction

The India–Asia collision zone—especially the Himalaya and the Tibetan Plateau (Fig. 12A)—has profoundly shaped our understanding of continent–continent collisions and orogenic plateaux evolution. Despite this prominence, processes at mid–deep crustal levels are not well understood because the Cenozoic mid to lower crust is exposed only locally within the Tibetan Plateau. In contrast, the Pamir (Fig. 12A) contain large exposures of mid to lower-crustal rocks in a series of domes (Robinson et al., 2004; Schwab et al., 2004; Schmidt et al., 2011; Stübner et al., 2013a). These domes—and the well-studied tectonic framework of the India–Asia collision—provide the opportunity to directly investigate mid to lower-crustal processes during the transition from thickening to collapse in an orogenic plateau. This paper presents a U-Pb titanite record of mid to lower-crustal exhumation and the implications for Pb and Zr retention in titanite, and proposes some possible driving mechanisms for gneiss-dome exhumation in the Pamir Plateau.

Orogenic plateaux may collapse when gravitational potential energy (GPE) overcomes compressive boundary forces (Molnar & Lyon-Caen, 1988; Rey et al., 2001; Selverstone, 2004). Changes in GPE come from changes in material thickness, elevation, and density. Significant changes in the boundary forces during continent–continent collisions may arise from processes such as slab breakoff, slab rollback, and foundering of convective instabilities. The rate of orogen collapse is determined by the imbalance of forces and material properties, which are dictated primarily by changes in temperature, composition, and phase (e.g., melting). In this paper, we assess whether collapse of the Pamir Plateau can be

Figure 12: A) The Pamir Plateau is the western extension of the India–Asia collision zone. B) The Yazgulom, Sarez, and Muzkol–Shatput domes of the Central Pamir, and the Shakhdara-Alichur dome in the South Pamir comprise the majority of the areal extent of the Pamir Plateau. Sample locations (yellow circles) were chosen to give the widest coverage possible. C) Earthquake locations show the position of subducting Asian lithosphere relative to the front of the Main Pamir Thrust zone (data from Sippl et al., 2013).

tied to changes in regional plate motions by measuring the U-Pb ages and trace-element contents (primarily Zr) of titanite in the Pamir mid–lower crust.

Titanite has some important advantages for dating crustal rocks: it occurs in a wide variety of rock types; it may grow or recrystallize during amphibolite-facies prograde and retrograde reactions (Rubatto & Hermann, 2001); it incorporates plenty of uranium in quartzofeldspathic rocks (Frost et al., 2001; Spencer et al., 2013); it partitions Zr as a function of pressure and temperature, enabling use as a thermobarometer (Hayden et al., 2008); and it participates in a wide variety of other metamorphic reactions (Frost et al., 2001). These qualities make it an ideal phase for investigating the history of the Pamir domes (Fig. 12B), which are dominated by amphibolite-facies quartzofeldspathic rocks (Vlasov et al., 1991; Robinson et al., 2004; Schwab et al., 2004). Recent analytical developments make coupled U-Pb + trace-element petrochronology (Kylander-Clark et al., 2013) a powerful tool for fingerprinting the timing and temperature of petrogenetic processes and more accurately understanding tectonic processes.

We show that titanite record a prograde/burial through retrograde/exhumation history in the Pamir gneiss domes from ~43 to ~8 Ma. Burial transitioned to exhumation at ~20 Ma, perhaps because of breakoff of the Indian slab. We relate high-temperature, exhumation-related metamorphism that persisted in the South Pamir until ~8 Ma to northward rollback of Asian lithosphere beneath the Pamir (Fig. 12C) or foundering of convective instabilities, and collapse of the margin of the Pamir Plateau into the adjacent Tajik Basin (Stübner et al., 2013a). Temperatures of nearly 700°C sustained for at least ~10 Myr were insufficient to

reset Pb and Zr in titanite, indicating higher closure temperatures than the commonly assumed range of 600–700 ºC.

Geologic Setting

The Pamir Plateau, the northwestern extension of the Tibetan Plateau, has a crustal thickness of ~60–75 km and an average elevation of ~4 km (Mechie et al., 2012; Schneider et al., 2013). Much of this thickening and uplift occurred during the India–Asia collision (Burtman and Molnar, 1993; Bershaw et al., 2012), driven by 600–900 km of Cenozoic shortening *within* the Pamir (Schmidt et al., 2011). The northern limit of the Plateau, the Main Pamir Thrust zone (Fig. 12B), accommodates 10–15 mm/yr present-day ~N–S shortening (Reigber et al., 2001; Mohadjer et al., 2010; Zubovich et al., 2010; Ischuk et al., 2013). This shortening is coupled to northwestward rollback of ~90-250 km of Asian lithosphere (the Pamir slab)—as inferred from receiver functions, local-earthquake tomography, and intermediate-depth seismicity (Schneider et al., 2013; Sippl et al., 2013a, 2013b). Presently, the down-dip end of this subducting Asian lithosphere is situated roughly beneath the southwestern Pamir (Fig. 12C). The southern limit of the Plateau, the Chitral Himalaya and Hindu Kush, accommodates a similar rate of shortening, 10–15 mm/yr (Mohadjer et al., 2010; Ischuk et al., 2013). The southern part of the Plateau is underlain to an unknown extent by underthrusting Indian lithosphere (Li et al., 2008; Sippl et al., 2013b). The interior of the Pamir shows 5–10 mm/yr of ~E–W extension that is matched by shortening in the Tajik Basin west of the Pamir; there is relatively little present-day motion between the Pamir and the Tarim Basin to the east (Mohadjer et al., 2010; Zubovich et al., 2010; Ischuk et al., 2013). Thus, material—in the form of the Indian slab and Asian lower crust—is flowing under the

Pamir Plateau from both the north and south while material flows north and west out of the Pamir interior over the Tajik Basin.

The modern ~E–W extension within the Pamir stands in contrast to the 600–900 km of long-term Cenozoic shortening within the Pamir, and indicates a distinct shift in kinematics that may—as intimated above—be linked to changes in GPE, boundary forces, or rheology. A series of large crystalline domes within the Pamir expose amphibolite-facies to granulite-facies rocks exhumed from depths of 30–40 km (Robinson et al., 2007; Schmidt et al., 2011; Stübner et al., 2013a,b). U/Th-Pb monazite and Lu-Hf garnet ages suggest that crustal thickening began ≥37 Ma in the Central and South Pamir (Schmidt et al., 2011; Stearns et al., 2013). A switch from burial to exhumation in the interior of the Pamir at ~20 Ma is implied by younger monazite ages (Stearns et al., 2013), and by detrital U-Pb zircon and $^{40}Ar/^{39}Ar$ white mica dates from modern river sediments (Lukens et al., 2012). Exhumation by ~N-S crustal extension is directly dated within the largest of the crystalline domes, the composite Shakhdara-Alichur dome of the South Pamir (Fig. 12B), at ~20–2 Ma (Stübner et al., 2013b). Peaking in the mid-Miocene and Pliocene, a thick wedge of coarse clastic sediment was shed into the Tajik Basin, suggesting loading of that basin by (north)westward growth of the Pamir (Schwab et al., 1980; Nikolaev, 2002).

The distribution of rocks within the Pamir Plateau defines three main units, the North Pamir, Central Pamir, and South Pamir (Fig. 12B)—all built and assembled during the Paleozoic and Mesozoic (Schwab et al., 2004).

North Pamir – Muztaghata-Kongur Shan dome

The North Pamir includes one Cenozoic dome: the Kongur Shan. The Kongur Shan dome exposes mid-Miocene metamorphic rocks exhumed from ~30 km depth by early ~N-S extension across the Shen-ti normal fault followed by ~E–W extension along the Kongur Shan extensional system (Brunel et al., 1994; Robinson et al., 2004 & 2007; Cao et al., 2013; Thiede et al., 2013). The core of the dome underwent crustal thickening and prograde amphibolite-facies metamorphism from ~33–20 Ma and reached peak metamorphic conditions in the early Miocene. Migmitization occurred at ~14 Ma, followed by exhumation of the Kongur Shan footwall through $^{40}Ar/^{39}Ar$ mica, U/Th-He in zircon (ZHe), and apatite fission track (AFT) closure occurred from ~8–1 Ma (Robinson et al., 2007; Thiede et al., 2013).

Central Pamir – Yazgulom, Sarez, & Muzkol-Shatput domes

The Central Pamir contains the Yazgulom, Sarez, and Muzkol–Shatput domes (Fig. 12B); the domes comprise folded and ductilely deformed (D_1 fabric) Paleozoic to Mesozoic marbles and siliciclastic rocks. Mesozoic and Cenozoic gabbroic to granitic intrusions were emplaced before and during regional shortening (Schwab et al., 2004; Stearns et al., 2013).

Prograde upper-amphibolite facies metamorphism (6–10 kbar and 600–750 ºC; Schmidt et al., 2011) occurred from ~30–15 Ma (Stearns et al., 2013) during the development of the D_1 fabric. Garnet amphibolites and kyanite + garnet + biotite ± staurolite metapelites are characterized by initial syn-deformation growth of garnet. The metapelites contain syn-kinematic kyanite and local staurolite as well, overprinted by post-kinematic kyanite and retrograde andalusite and sillimanite. The retrograde mineral assemblage within the

amphibolites is characterized by resorbed garnet, relict pyroxene, ilmenite and rutile breakdown to titanite, chlorite, and local retrograde biotite and amphibole growth.

Discordant Cenozoic aplite and pegmatite dikes and sparse intermediate to felsic plutons crosscut D_1 structures within the dome, and increase in abundance toward the dome cores. The dikes are typically non-deformed and contact metamorphosed their host rocks (e.g., static sillimanite overprint of kyanite). The deformation within the domes culminated in ~N-S extension that imprinted a mostly shallowly dipping, typically penetrative D_2 fabric that overprinted D_1. Mylonitized quartz and feldspar within the D_2 fabric typically transitions from ductile to brittle over 10–100s meters toward the dome-bounding normal-slip shear zones.

South Pamir – Shakhdara–Alichur dome

The South Pamir Shakhdara–Alichur domes expose the largest area of Cenozoic mid to lower-crustal rock in the Pamir. The South Pamir was inundated by arc magmatism during the Cretaceous and is dominated by orthogneiss and intrusive rocks (Schwab et al., 2004; Stübner et al., 2013a, b). The Cretaceous magmatic arc experienced contraction (D_1) prior to and synchronous with upper-amphibolite–granulite-facies metamorphism (5.5–15 kbar and 600–800 ºC; Schmidt et al., 2011) that culminated in extensive migmatization. The Shakhdara dome gneisses were exhumed by top-SSE shear along the ~30° south-dipping South Pamir shear zone (SPSZ), which bounds the dome in the south; flow occurred continuously from melt-present to brittle conditions. The Panj gorge exposes the footwall of the SPSZ in the core of the dome (Fig. 12B). The northern dome boundary comprises a mostly low-grade deformation belt, the Gunt shear/fault zone, where early top-to-~N

transtensional shear fabrics were folded into a subvertical zone and overprinted by dextral shear. The smaller Alichur dome is bounded in the north by the Alichur shear zone, which exhumed rocks from 10 to 20 km depth. The Shakhdara and Alichur domes are separated by a low-strain, fault-segmented horst (Fig. 12B). Cooling of the Shakhdara dome through $^{40}Ar/^{39}Ar$ mica closure began at ~20 Ma in the north (near the Gunt shear zone) and progressed southward from ~16 to 6 Ma along the dome-spanning SPSZ. NNE–SSW extension lasted until ~4–2 Ma (Stübner et al., 2013b), when it was replaced by active ~N–S shortening and ~E–W extension, imprinting the Sarez–Karakul graben system and distributed sinistral–transtensional faults across the western Pamir (Fig. 12B; Schurr et al., 2014).

Taxkorgan complex & Dunkeldik pipe belt

The Taxkorgan intrusive complex (Fig. 12B), in and adjacent to the southwestern margin of the Muzkol–Shatput dome, contains alkalic and granitic intrusive rocks ranging from ~13–8 Ma (Xu et al., 1996; Luo et al., 2003; Lin et al., 2006; Ke et al., 2006 & 2008; Robinson et al., 2007; Jiang et al., 2012). Jiang et al. (2012) interpreted the alkali magmas as lithospheric mantle melts, metasomatized by melt derived from a tearing or foundering slab at ~12 Ma.

The ultrapotassic Dunkeldik magmatic belt (Fig. 12B; Dmitriev, 1976) is located in the Central Pamir, southwest of the Muzkol-Shatput dome. The rocks range from dikes and pipes to sub-volcanic bodies and volcanic rocks. These rocks erupted at ~11 Ma (Hacker et al., 2005). The pipes contain crustal xenoliths comprising Pamir crustal rocks that had sunk to a depth of up to 90–100 km by either subduction or foundering (Hacker et al., 2005; Gordon et al., 2012).

Petrochronology method

By dating titanite associated with prograde and retrograde metamorphic reactions, and with the D_1 and D_2 deformation fabrics, the P-T-D-t paths can be extracted for each dome. The timing of prograde metamorphism was determined by dating titanite i) within locally generated leucosomes, ii) involved in prograde reactions such as the growth breakdown of ilmenite, and iii) included within prograde minerals such as garnet (Fig. 13A). The timing of retrograde metamorphism, interpreted as coeval with exhumation, was determined by dating titanite i) formed during retrogression of rutile and ilmenite (Fig 13B–D), and ii) dynamically recrystallized in the D_2 extensional fabric (Fig 13E). Igneous titanite from nondeformed aplite dikes was dated to place upper and lower bounds on the timing of extension (Fig. 13F). We measured U-Pb dates by LA-MC-ICP-MS (laser-ablation multicollector inductively coupled plasma mass spectrometry), U-Pb dates + trace elements by LASS (laser ablation-split stream ICP-MS), and additional Zr contents by EPMA (electron probe microanalysis).

LA-MC-ICP-MS & LASS

Sixty samples were analyzed from the four gneiss domes (Fig. 12B, Appendix 6). The majority of samples were dated using LA-MC-ICP-MS; a subset was dated using LASS (Kylander-Clark et al., 2013). Typical excimer laser (193 nm wavelength) settings were 30–100% of 3 mJ, 4 Hz repetition rate, and a 25–40 μm diameter laser spot. Bear Lake Road titanite (Aleinikoff et al., 2002; Frost and Fanning, 2006; Mazdab, 2009) was used as the primary reference material and Y1710C5 (Spencer et al., 2012) was used as the secondary reference material to assess in-run accuracy. The dates reported in this paper have a minimum uncertainty of 2%. For more analytical details, see Spencer et al. (2013).
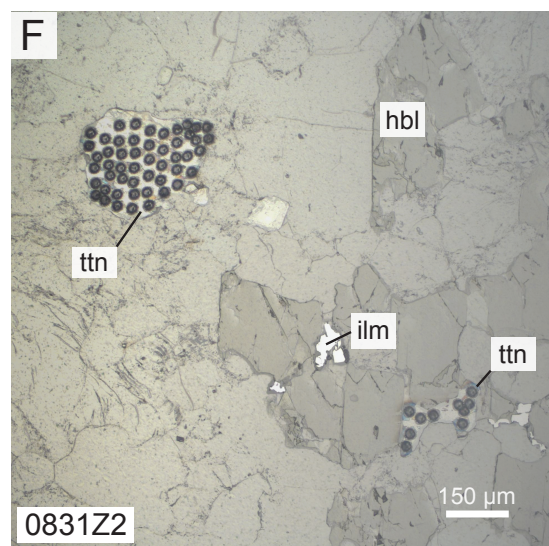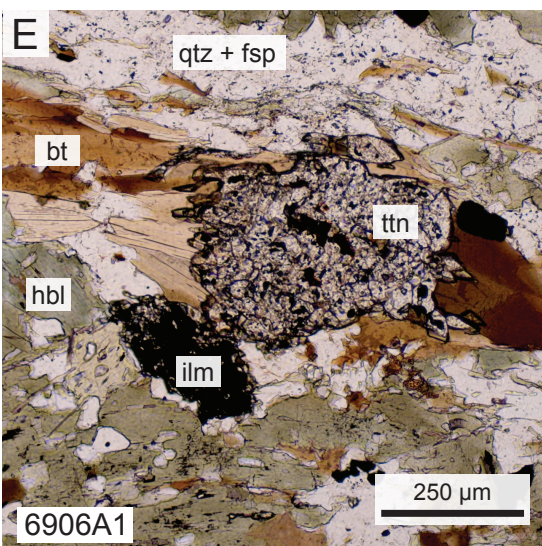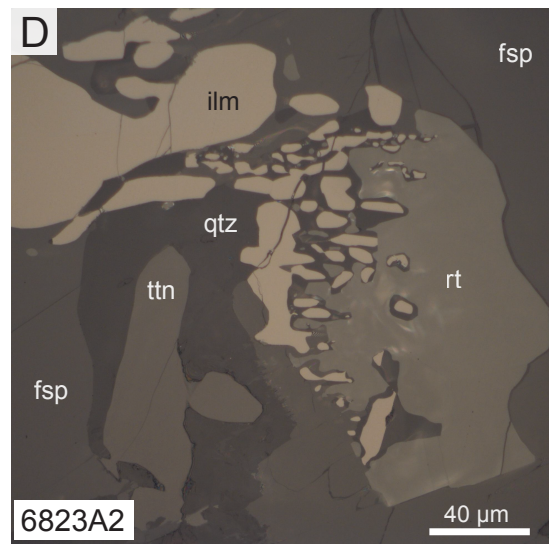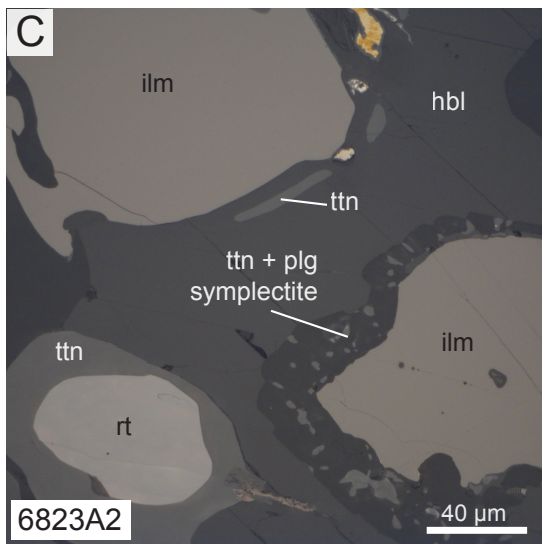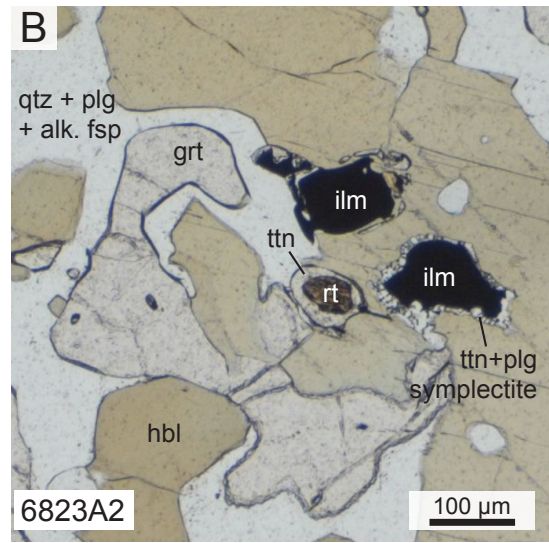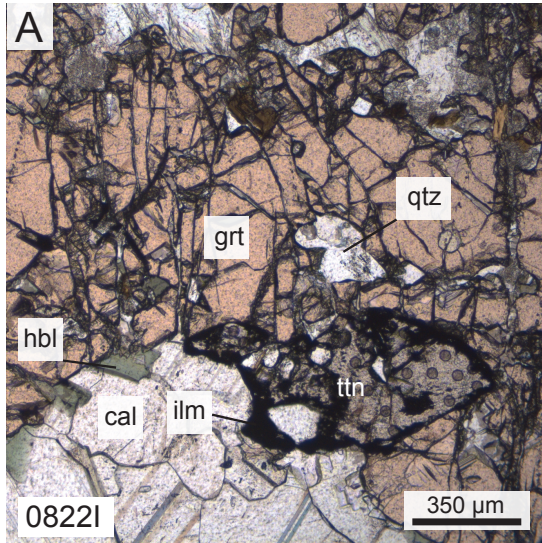
Figure 13: Titanite textures in thin section. A) 32.4 ± 0.8 Ma titanite breaking down to ilmenite and partly included within garnet are interpreted to date prograde metamorphism in Yazgulom dome. B, C & D) Retrogressed mafic amphibolite after garnet granulite that is interpreted to have melted based on the reaction rims and acute grain boundaries. B) 8.9 ± 0.4 Ma single-age titanite forms retrograde rims on rutile and ilmenite. C) 8.9 ± 0.4 Ma titanite formed by breakdown of rutile and ilmenite. D) Complex reaction textures between coexisting rutile, ilmenite, and titanite illustrate the difficulty of determining a single titanite forming reaction. These titanites are interpreted to record decompression melting during retrograde metamorphism of the southern Shakhdara dome. E) Dynamically recrystallized titanite porphyroclast formed by the breakdown of ilmenite. 19.5 ± 0.4 Ma age is interpreted to record onset of exhumation in Yazgulom and the timing of high-T extensional deformation. F) Titanites between ~100–400 μm with many spots yielded a single age of ~17.3 ± 0.5 Ma. These titanites within a group of float boulders from the far western Muzkol–Shatput dome formed by breakdown of ilmenite during retrograde metamorphism.

The majority of samples were analyzed in situ in thin section; seven samples were analyzed as titanite separates. Twenty to eighty single spots were analyzed from several grains per sample. Different grain sizes and different portions of large grains were analyzed to allow an assessment of the variations in age. Titanite zoning was imaged using backscattered electrons (BSE). Where zoning was detected, laser spots were placed entirely within zones to minimize mechanical mixing.

Electron probe microanalysis (EPMA)

Zirconium concentration was measured in titanite with a Cameca SX-100 at 15 kV accelerating voltage and 200 nA beam current. Bear Lake Road titanite (Aleinikoff et al., 2007; Mazdab, 2009; Spencer et al., 2013) and NIST 610 glass (Gao et al., 2007) were used as secondary reference materials. Atomic number, absorption, and fluorescence (ZAF) corrections were made assuming an ideal $CaTiSiO_5$ composition. The Zr detection limit was ~10–20 ppm. For further analytical details, see Spencer et al. (2013). Measurement of Zr in titanite is susceptible to secondary fluorescence from zircon: a linear transect away from a ~30 μm diameter zircon showed that secondary fluorescence is significant to a distance of ~40 μm, but negligible more than ~100 μm from the zircon. The area around each titanite Zr measurement was therefore carefully screened for zircon; it is possible, however, that secondary fluorescence affected some of the Zr measurements from out-of-plane zircon.

The Zr-in-titanite thermometer is pressure dependent (Hayden et al., 2008). Though peak pressures are known for many of the samples by independent determinations (Schmidt et al., 2011), the quoted apparent temperatures were calculated using a pressure of 4 ± 2 kbar because most titanite (re)crystallization occurred during retrograde metamorphism. Two

uncertainties were calculated: one that includes analytical error and the reproducibility of the secondary reference materials, and a second that includes uncertainty in pressure and the activity of $CaZrSiO_5$; all the thermometry samples contain quartz, zircon, and rutile. Zr thermometry provides not only an apparent temperature, but also can be used to distinguish distinct titanite populations and provide further petrogenetic context for interpretation of U-Pb dates.

Results

A summary of the titanite U-Pb dates is shown in Figure 14; all of the U-Pb data are provided in Appendix 6. We classify our U-Pb dates into three types (Fig. 15). 1) **Single ages**, in which all of the U-Pb data define a single isochron with a suitably low MSWD to be a single population (Wendt and Carl, 1991); for such samples we report a single age and uncertainty (Fig. 15A). 2) **Multiple ages**, in which the U-Pb data define multiple isochrons (Fig. 15B), each of which has a suitably low MSWD to be a single population. For such samples, multiple ages and uncertainties are reported. 3) **Age ranges**, in which the U-Pb data do not define an isochron or isochrons; for these data we report a range of "^{207}Pb-corrected" (sensu Compston, 1992) ^{206}Pb/^{238}U dates (Fig 15C).

Because titanite is often considered to have a whole-grain closure temperature of ~600–700 °C (see review in Spencer et al., 2013), one might expect that amphibolite-facies titanite would routinely show grain-scale gradients in age or that bigger titanite would preserve older ages. Like Spencer's Norwegian titanites, however, this is not the case for the Pamir titanites—at least at the scale of our laser spots. Instead, we observe four different relationships between age and grain size or position within grains (Fig. 16). 1) Pamir titanites
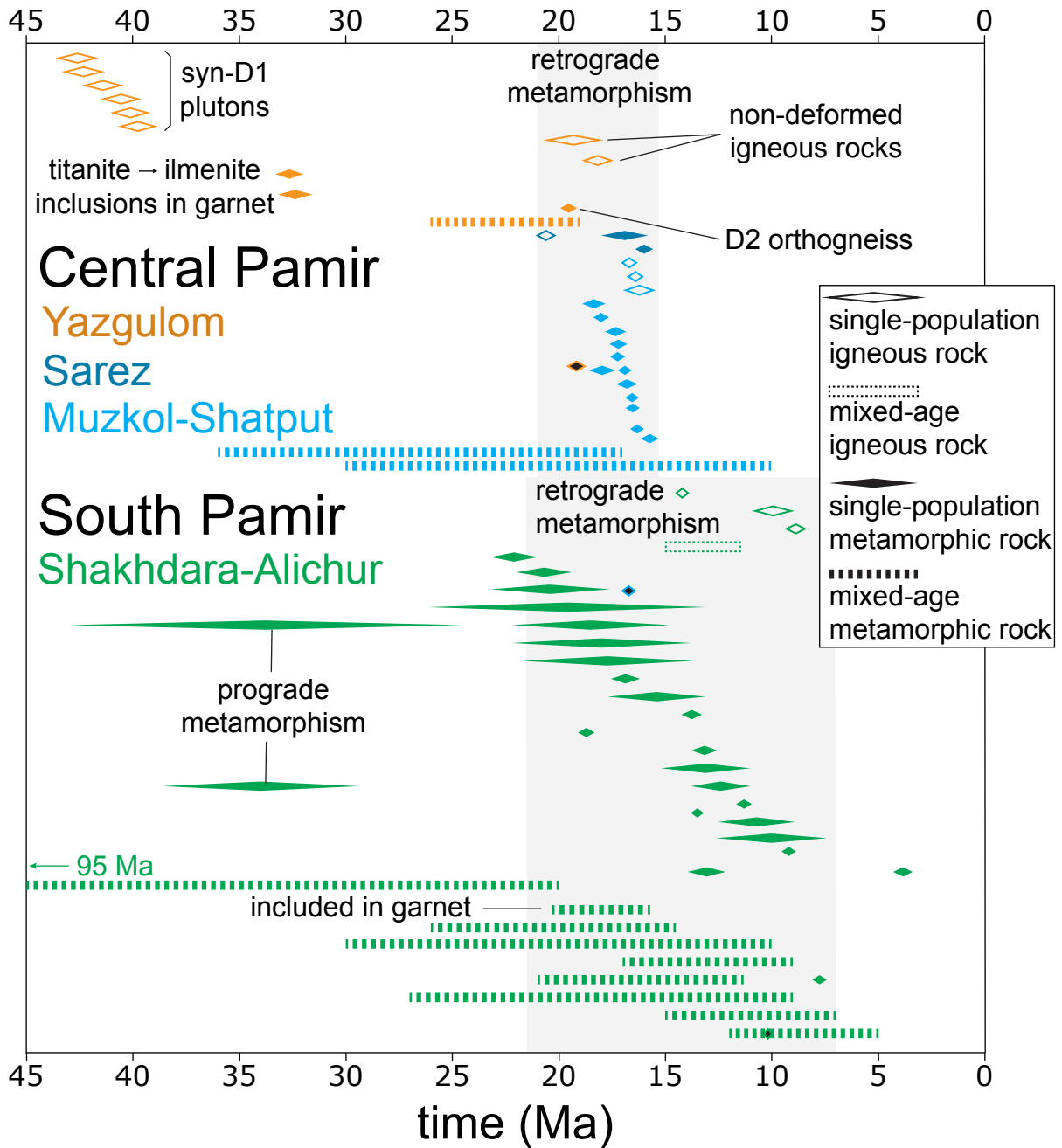
46

Figure 14: U-Pb titanite dates from the Pamir. Igneous titanite crystallized in the Central Pamir from 43–40 Ma. Titanite records prograde metamorphism in the Central and South Pamir around 33 Ma. Retrograde titanite (re)crystallized in the Central Pamir during exhumation (grey bands) from 21–15 Ma; more-protracted retrogression and exhumation in the South Pamir was recorded by 22–7 Ma titanite. Black filled ages are previously published in Schmidt et al. (2011).
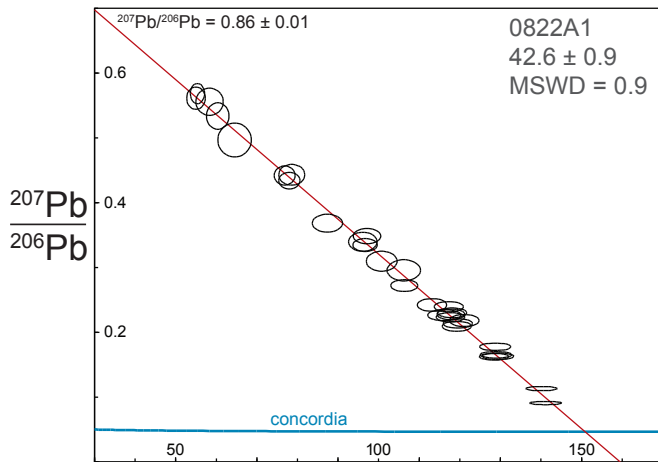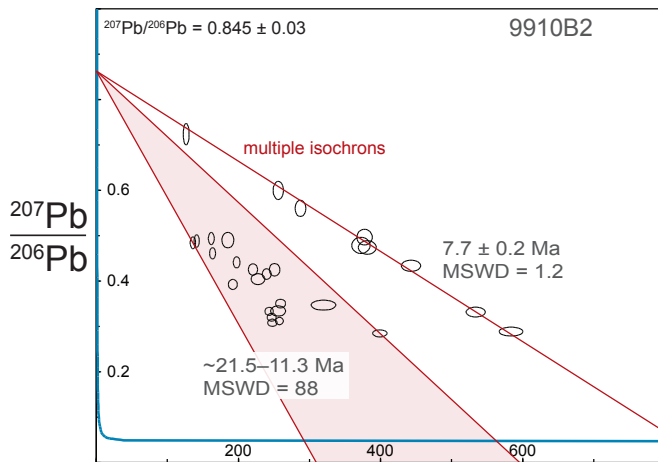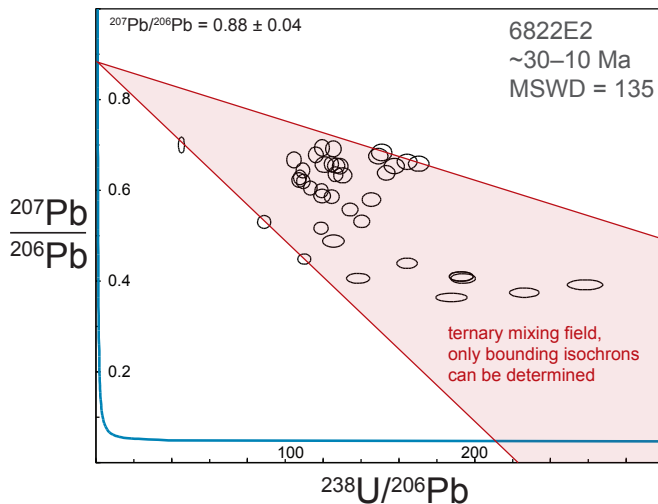
A. Single age

$^{207}Pb/^{206}Pb = 0.86 \pm 0.01$

0822A1
42.6 ± 0.9
MSWD = 0.9

$\dfrac{^{207}Pb}{^{206}Pb}$

0.6
0.4
0.2

concordia

50   100   150

B. Multiple age

$^{207}Pb/^{206}Pb = 0.845 \pm 0.03$

9910B2

multiple isochrons

$\dfrac{^{207}Pb}{^{206}Pb}$

0.6
0.4
0.2

7.7 ± 0.2 Ma
MSWD = 1.2

~21.5–11.3 Ma
MSWD = 88

200   400   600

C. Age range

$^{207}Pb/^{206}Pb = 0.88 \pm 0.04$

6822E2
~30–10 Ma
MSWD = 135

$\dfrac{^{207}Pb}{^{206}Pb}$

0.8
0.6
0.4
0.2

ternary mixing field,
only bounding isochrons
can be determined

100   200

$^{238}U/^{206}Pb$

Figure 15: Titanite preserve three different types of U-Pb ages. A) Single ages, with isotopic ratios that form a single population (MSWD ~1). B) Multiple ages, defined by multiple, single-population arrays. C) Age range, characterized by ternary mixing between a common-Pb component and multiple radiogenic-Pb components; this can result from continuous (re)crystallization or mechanical mixing during laser sampling.
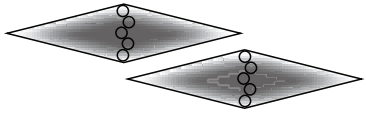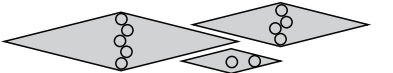
48
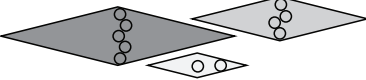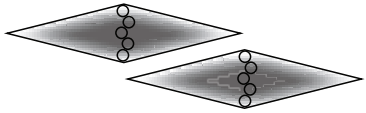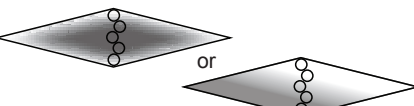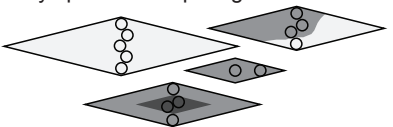
expectations for closure ages	closure-age tests for in situ petrochronology	
1) age covaries with grain size	observations	interpretations
	1) range of grain size & single age	i) de novo crystallization
		ii) complete recrystallization
2) age covaries with spot position	2) same grain size, but many spots & single age	i) de novo crystallization
		ii) complete recrystallization
	3) same grain size, but many spots & age range	i) prolonged (re)crystallization
		ii) incomplete recrystallization
old young	or	iii) volume diffusive loss of Pb
	4) many spots & multiple ages	i) partial recrystallization
		ii) multiple crystallization events

Figure 16: If a sample's age results from mineral closure, the grain age would co-vary with grain size and spot position. These hypothetical relationships can be tested by in situ petrochronology by the placement of laser spots that are much smaller than the grain diameter and analyzing a range of grain sizes (larger than the analysis spot).

with a range of grain sizes that all yield the same age are interpreted to record de novo crystallization or complete recrystallization at temperatures too low for diffusional re-equilibration (Fig. 13A & F). 2) Titanites of a similar size and large enough to accommodate multiple laser spots that all yield the same age are also interpreted to record de novo crystallization or complete recrystallization. 3) Titanites of a uniform grain size that yield an age range may have undergone i) prolonged de novo crystallization, ii) incomplete or prolonged recrystallization, or iii) cooling through a temperature interval conducive to Pb diffusion. 4) Titanites large enough for multiple laser spots that yield multiple ages are interpreted to record multiple crystallizations or partial recrystallization at a scale larger than the 25–40 μm laser spot.

Central Pamir petrochronology

In the carbonate and orthogneiss-dominated **Yazgulom dome** (Fig. 17A), 12 samples were dated. Two garnet amphibolites (0822I1 & 0822I2) yielded single ages of ~33 Ma from titanite within the matrix and included within garnet (Fig. 13D). The amphibolites are likely part of the 500–450 Ma bimodal igneous sequence that forms the core of the dome (Schwab et al., 2004). Seven granitic intrusions yielded single-age titanite spanning ~43–39.5 Ma (8022A, 0822X & Y, 6907B & C) to ~20.5–17.5 Ma (4727J & 9922A). Titanites from two mylonitic (normal-sense D_2 fabric) samples record a single age of 19.5 ± 0.2 (orthogneiss 6906A) and an age range of ~26–19 Ma (paragneiss 11923E). We interpret the Yazgulom titanite dates to record granitoid emplacement from at ~43–39.5 Ma and amphibolite-facies metamorphism at ~33 Ma. Regional metamorphism was followed by granitoid emplacement from ~20.5–17.5 Ma, synchronous with the onset of extensional deformation at ~26–19 Ma.
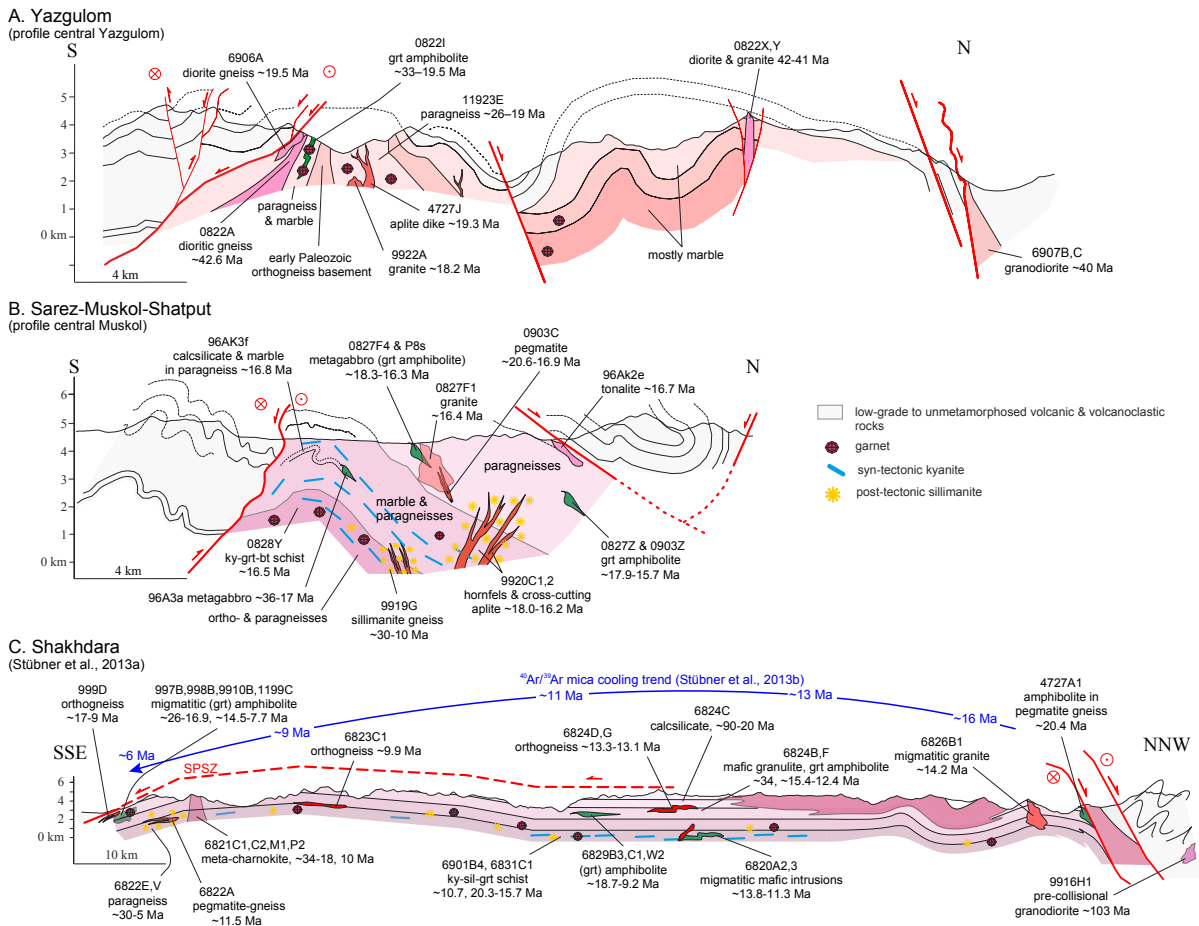
Figure 17: Diagrammatic cross sections placing the analyzed titanites within the structure and lithology of the domes. A) Yazgulom dome: ~40 Ma orthogneiss are overprinted by metamorphism and magmatism from 39 to 18 Ma. B) Sarez–Muzkol–Shatput domes: 36–30 Ma metamorphic rocks overprinted by mostly 20–16 Ma metamorphism and magmatism. C) Shakhdara dome: 34–30 Ma gneisses overprinted by mostly 20–8 Ma metamorphism and magmatism. Cross sections modified from Stübner et al. (2013b) and Rutte et al. (2013).

Two samples from the **Sarez** dome were dated (these samples are included in the section across the central Muskol dome, Fig 17B, because the overall structure of these domes is similar): a contact-metamorphosed garnet amphibolite (0903Z) that is crosscut by two km-scale intrusions within the core of the dome and by a crosscutting pegmatite dike (0903C). Titanite grains from the amphibolite have a single age of 16.0 ± 0.4 Ma. A 12 mm titanite from the crosscutting dike yielded multiple ages: 20.6 ± 0.4 and 16.9 ± 1.1 Ma. These ages correspond to BSE-pale and BSE-dark zones, and are interpreted as emplacement and recrystallization ages, respectively. The titanite ages are interpreted to record dike emplacement at ~20.6 followed by contact metamorphism of the amphibolite and dike at ~16 Ma.

Fifteen samples from the **Muzkol-Shatput** dome were dated (Fig. 17B). Garnet amphibolites (0827F4, P8s, 96AK3A & 0827Z) that form the wall rock to intrusions and are crosscut by dikes have rutile and ilmenite retrogressed to titanite; the titanite yield an age range of ~36–17 Ma and single ages from ~18.5–15.5 Ma. Calcsilicates, schists, and paragneisses contain single-age titanites (0828Y3, 96AK3F, 9920C2) from 18.4–16.2 Ma and one age range of ~30–10 Ma (9919G). Granitoids and dikes, that crosscut the amphibolites and metasediments across the dome, have single-age titanites from 16.8–15.5 Ma. We interpret the tightly clustered amphibolite dates to record retrograde metamorphism from ~18.5–15.5, closely followed by dike emplacement at ~16.8–15.5 Ma.

Central Pamir titanites have either homogeneous Zr contents or Zr-rich cores and Zr-poor rims. The cores range from ~200–500 ppm Zr and are interpreted to be inherited. The homogenous titanites and rims have ~75–175 ppm Zr (blue data; Fig. 18A) and are
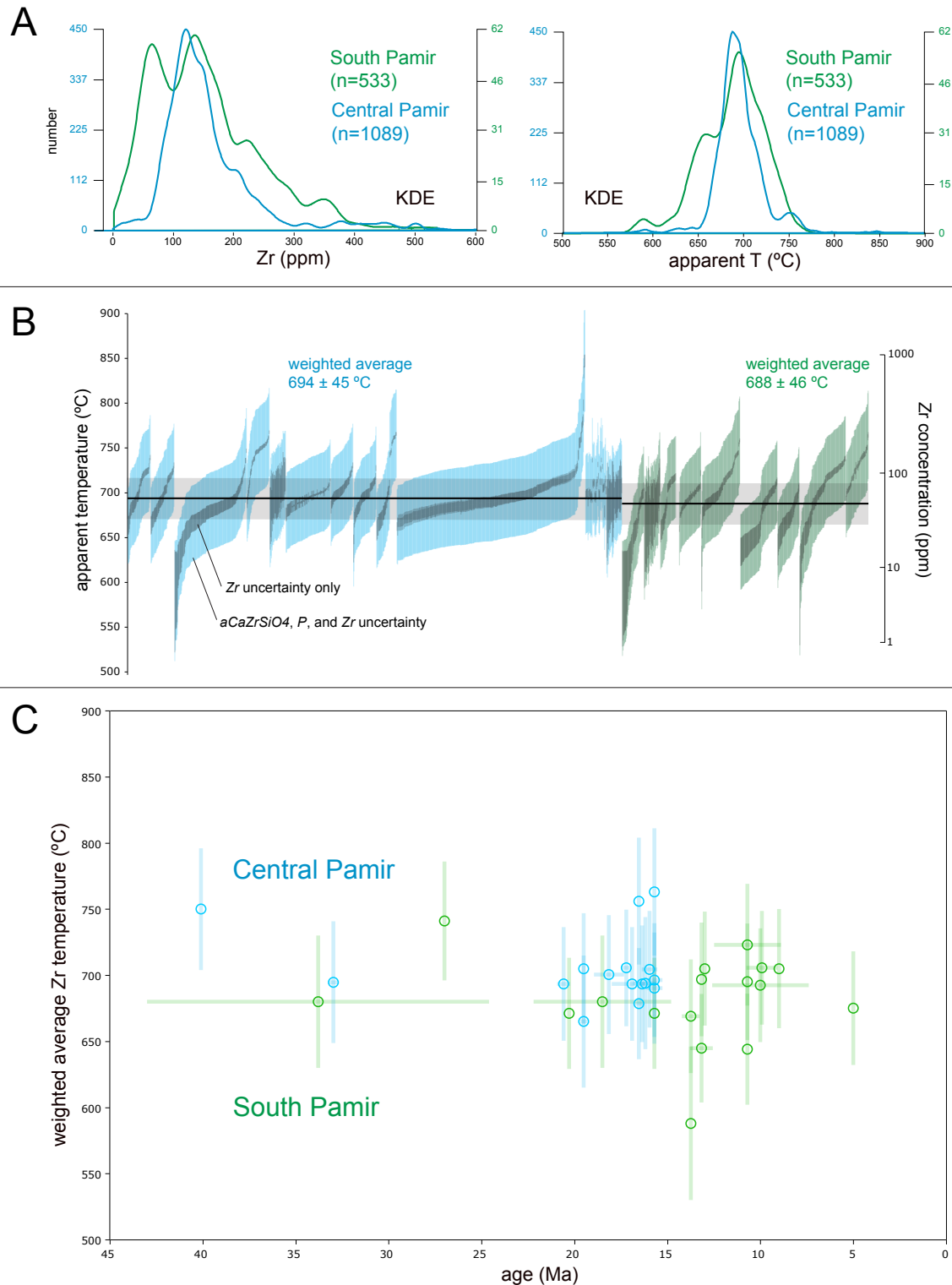
Figure 18: The Zr contents in titanite and Zr-in-titanite temperatures (Hayden et al., 2008) are similar in the Central and South Pamir, and indicate (re)crystallization at amphibolite-facies conditions. A) all data; B) data for individual samples. C) The temperature–time history shows prolonged amphibolite-facies conditions that persist until ~7 Ma in the Shakhdara dome.

interpreted to reflect amphibolite-facies retrogression. Despite these petrogenetic differences, the Zr contents correspond to apparent temperatures that overlap within uncertainty: the weighted mean apparent temperature at 4 ± 2 kbar of all samples is 694 ± 45 ºC (Fig. 18B; MSWD = 1.1). These apparent temperatures are interpreted as temperatures of titanite (re)crystallization. If a titanite equilibrated during prograde or peak pressures of 8 ± 2 kbar instead of 4 ± 2 kbar is used in the calculation, the resulting apparent Zr temperature would be 30–40 ºC higher but still within the quoted uncertainty.

South Pamir petrochronology

Thirty-one samples from across the **Shakhdara–Alichur** dome were analyzed (Fig 17C); twenty-six metamorphic rocks and five igneous rocks. The titanites record 1) pre-collision igneous intrusion (9916H, 6823A2), 2) prograde metamorphism from ~34–25 Ma (6821C1 & 6824F1), 3) nearly continuous retrograde titanite growth (from rutile and ilmenite) from ~25–9 Ma, and 4) aplite and pegmatite dike emplacement from ~15–8 Ma (6820A, 6823A2, 6823C1, 6826B1 & 6822A3). In general, the titanite dates young toward the South Pamir shear zone (SPSZ; Fig. 19A).

The dates come from four different structural domains identified by Stübner et al. (2013a) (Fig. 12B): the Gunt shear zone (GSZ), SPSZ, Panj Gorge dome transect (PGT), and central Shakhdara dome. The youngest titanite dates (i.e., a single age or the lower bound of an age range) from the PGT correlate with elevation (Fig. 19B). Age–elevation trends (proxy for exhumation rate) do not include all the data, but rather were calculated from the 'leading edge' of the ages. The youngest SPSZ titanites range from ~17–7 Ma and span ~2250 m. These data overlap the $^{40}Ar/^{39}Ar$ dates (Stübner et al., 2013) and have a similar slope of ~0.25 ± 0.05 mm/yr. Samples from the PGT range from ~15–8 Ma and span ~2250 m (~1.1
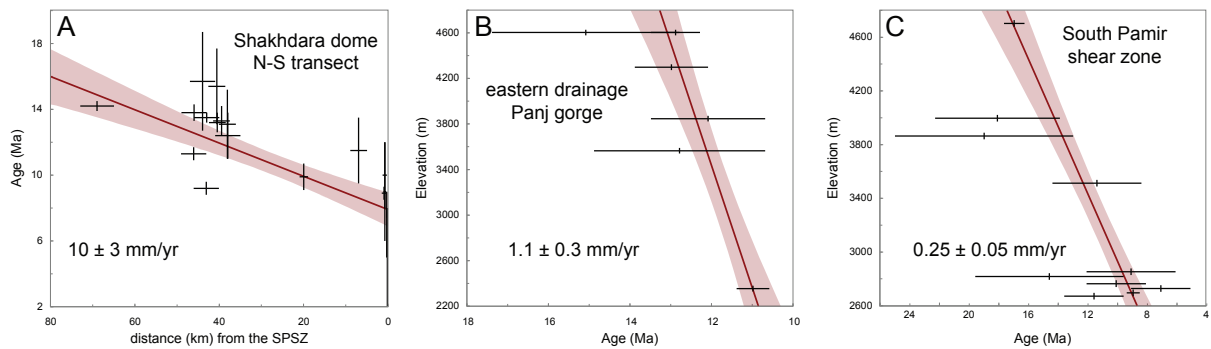
Figure 19: Age–distance from U-Pb titanite (crosses) from a (A) NNW–SSE transect across the Shakhdara dome and age–elevation transect through (B) the core of the Shakhdara dome (eastern Panj gorge) and (C) near the South Pamir shear zone show similar long-term cooling trends to the $^{40}Ar/^{39}Ar$ mica ages (Stübner et al., 2013b). The plotted titanite data are either single ages or the youngest of multiple ages or age ranges from the relevant samples.

± 0.3 mm/yr). The titanite dates are older than the $^{40}Ar/^{39}Ar$ ages by ~3–4 Myr along the PGT and the exhumation rate (1.1 ± 0.3 mm/yr) is faster than the thermochronology determined exhumation rate of 0.4 ± 0.2 mm/yr.

In summary, titanite from Shakhdara records prolonged high-temperature retrograde metamorphism and migmatization related to tectonic unroofing by ~NNE-SSW extension from ~15–8 Ma, only slightly predating the ^{40}Ar-^{39}Ar cooling ages.

Titanites from the South Pamir contain ~10–475 ppm Zr (Fig. 18A). Both high-Zr cores/low-Zr rims and low-Zr core/high-Zr rims are present in single-age samples and in samples with an age range. In general, samples with U-Pb ages between ~20–13 Ma have ~60–150 ppm Zr, whereas samples younger than ~12 Ma have ~140–250 ppm Zr. The weighted-mean apparent temperature of the ~20–13 Ma population is 671 ± 43 ºC (MSWD = 0.6) and the <12 Ma population is 703 ± 45 ºC (MSWD = 0.3). Again, if peak pressures were instead used for the calculation the resulting apparent temperature would be ~30–40 ºC higher, but still within uncertainty. These apparent temperatures record heating and/or decompression after ~12 Ma.

Coupled U-Pb and trace-element analysis of samples 997B3 and 6822V1 (Fig. 20 & 21) shows intra-sample chemical variations that correlate with age. Maps of representative clusters of analyses from sample 997B3 (Fig. 21A) and sample 6822V1 (Fig. 21B) show the spatial relationship of the trace element–age variability. Though sample-wide analyses of sample 997B3 vary continuously from ~27 Ma domains with high Zr, Y, and Sr content to ~7 Ma domains with low Zr, Y, and Sr (Fig. 20), the maps show that the end-member domains are often adjacent to one another. As a whole, the variation is continuous but nonlinear. It
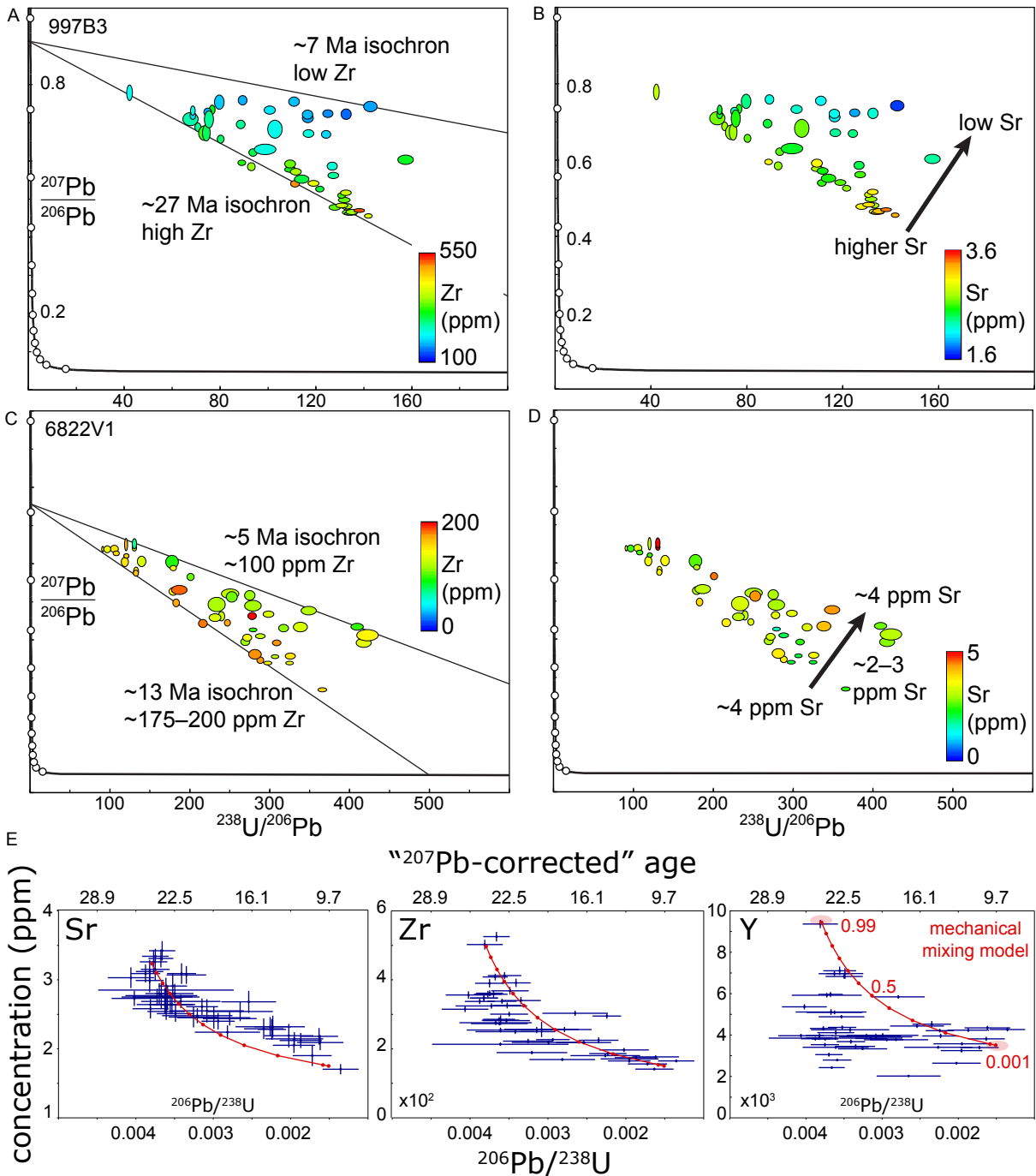
Figure 20: Coupled U-Pb and trace element analysis from two samples show variation in both A & B) Zr and C & D) strontium (Sr) through time. Variation due to mechanical mixing or contamination by inclusions is unlikely because the mixing of chemical or isotopic end members fail to account for the observed trajectories that the majority of the data define. E) An element-isotopic ratio mixing model shows that only some of the variation (e.g. Sr and Zr) can be attributed to mechanical mixing during laser ablation while the variation of yttrium is not likely to have been caused by mixing during sampling. Each end member is shown by a red ellipse and the proportion of the lower end member is labeled for Y.
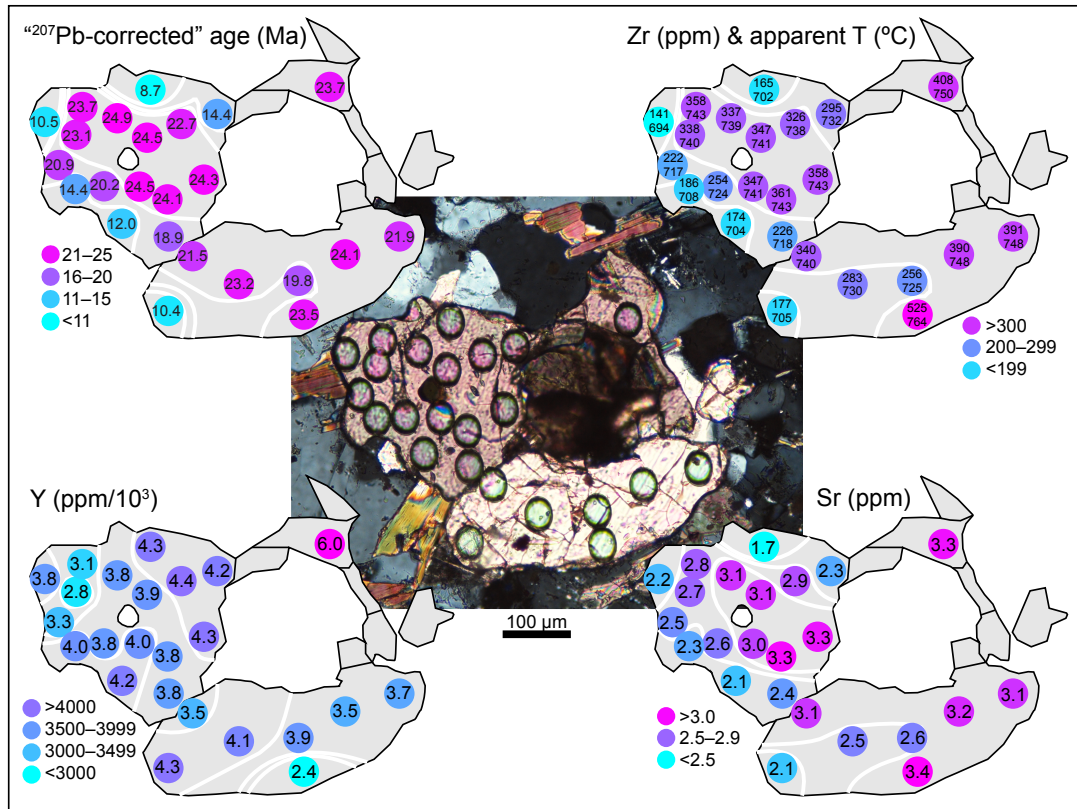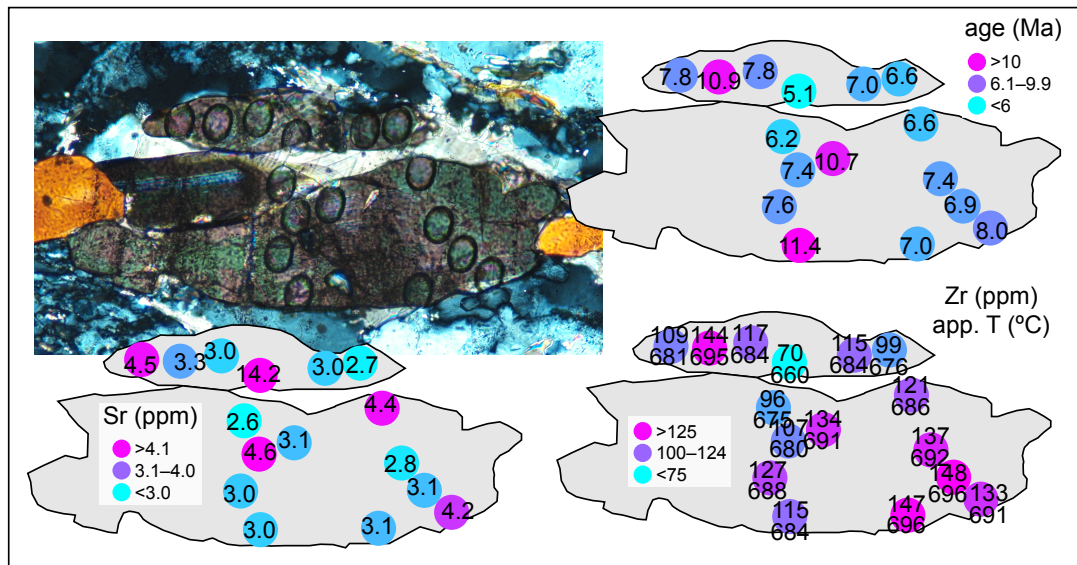
Figure 21: Maps and photomicrographs of a representative cluster of analyses show the spatial relationships between age and trace element compositions. A) Sample 997B3 has an older core with generally higher Zr, Y, and Sr. B) The maps of sample 6822V1 do not show such a clear correlation with age and trace element content. In both samples the trace-element content, age, grain sizes, and spot positions do not follow the predictions outlined in Fig. 4 and thus are interpreted as incomplete or prolonged recrystallization.

was compared to a mixing model to evaluate whether it resulted from mechanical mixing during laser ablation. Though some individual data fall on the mixing curve, the mixing model fails to predict the trace element trajectory for Y and Zr, and only fits a portion of the Sr data, suggesting that the elemental variation is the result of continuous reaction or recrystallization and not mechanical mixing. The grains maps of sample 997B3 in Fig 21A are consistent with the concordia plots (Fig. 20A-B) and show that: 1) most older analyses are within the grain cores, but some are near grain rims and 2) the smallest grains are not the youngest. These observations are similar to those outlined in the Figure 16 (#4, center column) and thus are interpreted to record partial or continuous recrystallization at ~20–6 Ma.

Similarly, sample 6822V1 (Fig. 20C & D; 21B) yielded continuous U-Pb dates from ~13–5 Ma that decrease from ~200 to 100 ppm Zr; unlike 997B3, the Sr content decreases from ~4 to 2 ppm, then increases back to 5 ppm. This pattern in sample 6822V1 could not have been formed by either mechanical mixing or volume diffusion and is interpreted as prolonged titanite (re)crystallization. The grain maps of an aggregate of titanites from sample 6822V1 (Fig. 21B) shows similar relationships to 997B3 between grain size, proximity to grain boundary, and resetting and are also interpreted to record partial or continuous recrystallization from ~13–5.

Discussion

Titanite closure

Evaluating the role of volume diffusion is an important aspect of understanding the processes that control U-Pb ages and the distribution of Zr. Experiments have shown that volume

diffusion of Pb (Cherniak 1993; Cherniak, 2010) is roughly two orders of magnitude faster than Zr (Cherniak, 2006; Hayden et al., 2008). Both experimental and natural datasets indicate that volume diffusion of Pb and Zr should occur at amphibolite-facies conditions (e.g., Scott and St-Onge, 1995; Corfu, 1996; Cherniak, 2006). For Pamir metamorphic temperatures of ~700°C and durations of ~20 Myr, Pb should have been completely lost from ~1000 μm grains, and larger grains should show Pb zoning at the ~50 μm scale. In contrast to this expectation, titanite from the Pamir retained both Pb and Zr over a prolonged period from >30 Ma to ~7 Ma (e.g. samples 0822I, 96AK3, and 6824F).

Nearly all the samples analyzed in this study contain roughly an order of magnitude variation in titanite grain size (Fig. 13F, 21A & B; ~25–400 μm diameter). Many of the samples with a range of titanite grain sizes yielded single ages within the spatial resolution of the laser spots (30–40 μm). For the observed range of grain sizes (~50–500 μm), a cooling rate >200 ºC/Myr is required (Cherniak, 1993). This hypothetical cooling rate is faster than the ~50–75 °C/Myr thermochronology-determined cooling rates from the Pamir (Stübner et al. 2013b).

Pamir plate-tectonic events

Following the initial breakoff of the oceanic part of the Indian slab subducting beneath Asia (Fig. 22A; Kohn and Parkinson, 2002; Negredo et al., 2007) at ~45 Ma, subduction of a buoyant Indian plate is inferred to have forced the Asian plate into contraction (Chung et al., 2003; Replumaz et al., 2010; DeCelles et al., 2011). Then, beginning at 32–25 Ma, the lower crust and mantle of the Indian plate is interpreted to have rolled back southward (Ding et al., 2003; Chung et al., 2005; Kapp et al., 2007). This is thought to have culminated at ~25–20
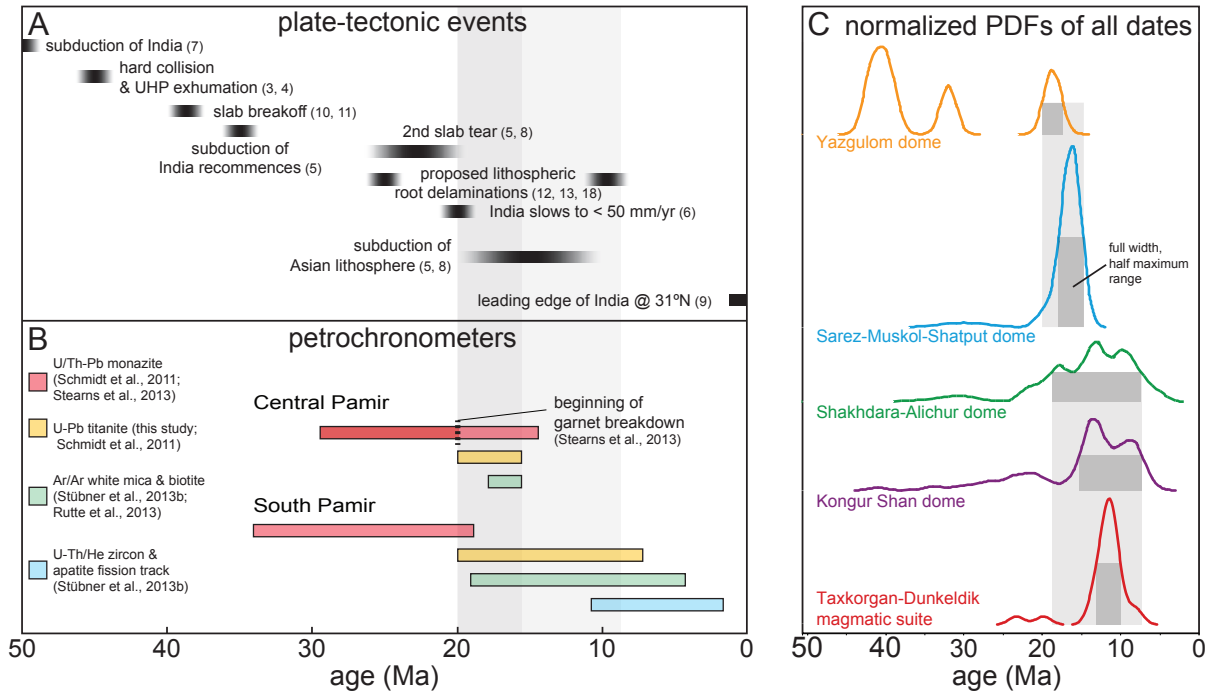
Figure 22: Comparing the petrochronologic record (B) to independently identified plate-tectonic (A) events shows any possible driving mechanisms of the metamorphism and later exhumation of the Pamir domes. Titanite petrochronology (yellow boxes and shaded bars) from this study place limits on the timing of the transition from thickening to exhumation. C) Normalized probability density function of all of the published U-Pb and Ar/Ar geocrhonology from each of the Cenozoic Pamir domes and the Taxorgan-Dunkeldik volcanic complex illustrates the differences between timing of metamorphism and exhumation of the Yazgulom-Sarez-Muzkol-Shatput domes inferred to be driven by Indian lithospheric delamination and the Shakhdara-Kongur Shan-Taxorgan events interpreted to be driven by rollback of the Pamir slab.

Ma in a second breakoff of the underthrust Indian continental slab (Replumaz et al., 2010; DeCelles et al., 2011).

In the Pamir, shortening across the Main Pamir Thrust zone and large-scale dextral strike-slip along its eastern margin commenced at 25–18 Ma (Sobel and Dumitru, 1997; Coutand et al., 2002; Cowgill, 2010) or ~10–6 Ma (Bershaw et al., 2012; Cao et al., 2013). As rollback of the Asian lithosphere beneath the Pamir is likely partly accommodated by thrusting along the Main Pamir Thrust (Sippl et al., 2013b; Sobel et al., 2013), the rollback probably started not earlier than 25–18 Myr ago.

U/Th-Pb monazite ages document prolonged metamorphism from 35–20 Ma in the South Pamir and 29–14 Ma in the Central Pamir (Fig. 22B; Schmidt et al., 2011; Stearns et al., 2013). Depletion in heavy-rare earth element (HREE) contents of monazite from the Central Pamir suggests decompression at ~20 Ma. Titanite ages from this study (Fig. 13) associated with cooling/decompression reactions record the beginning of exhumation from ~20 Ma in the Central and South Pamir. Central Pamir titanite ages overlap with ^{40}Ar/^{39}Ar mica cooling ages from the Muzkol–Shatput dome (Rutte et al., 2013), suggesting cooling from ~675–750 ºC (Zr apparent temperatures) through muscovite closure (~350–300 ºC) in less than 5 Myr. In contrast, titanite from the South Pamir record prolonged and later peak (re)crystallization at temperatures ≥ 650 ºC until ~7 Ma (Fig. 22B).

The timing of Shakhdara high-temperature exhumation is similar to the exhumation interval of the Kongur Shan dome and the eruption ages of the Taxkorgan–Dunkeldik subvolcanic and volcanic rocks (Fig. 22C). Th-Pb monazite ages and ^{40}Ar/^{39}Ar mica ages from the

footwall of the Kongur Shan extensional system record metamorphism from ~30–20 Ma followed by migmatization at ~14 Ma and exhumation from ~11–8 Ma. Th-Pb ages from monazites within garnet have a different distribution (~25 Ma mode) than monazites in the rock matrix, which are predominantly younger than ~18 Ma.

The Taxkorgan alkalic complex (Lou et al., 2003; Ke et al., 2008) and Dunkeldik volcanic field (Ducea et al., 2003; Gordon et al., 2012) have eruptive ages between ~23–8 Ma with the mode at ~11 Ma (Fig. 22C). The common ages of these volcanic complexes and of the rapid exhumation of the Shakhdara and Kongur Shan domes suggest that the volcanism and extension were triggered by the same event. Jiang et al. (2012) suggested that the Taxkorgan and the Dunkeldik suite magmas both resulted from decompression melting and asthenosphere upwelling following a slab breakoff.

Combining these inferences with seismic imaging (Mechie et al., 2012; Schneider et al., 2013; Sippl et al., 2013b), leads to the following possible tectonic evolution. 1) Northward subduction of Tethyan oceanic lithosphere is followed by collision and subduction of Indian continental lithosphere. 2) Breakoff of the Indian oceanic lithosphere occurred at ~45 Ma. Subsequent continuing contraction thickened the Pamir crust from ~37–20 Ma. 3) Subduction of Indian continental lithosphere continued until a second rollback and breakoff of the Indian lithosphere beginning ~25–20 Ma. 4) Indian continental lithosphere break-off, perhaps accompanied by downwelling and convective removal of a dense Asian lithospheric root, resulted in a regional increase of GPE in the Pamir and likely the Hindu Kush and Karakoram further south. Both downwelling and increased GPE may have triggered delamination and rollback of the Asian continental lithosphere (Pamir slab), which drove the

63

Pamir crust from contraction into extension ~20 Ma ago. This change in boundary forces lead to rapid cooling of the mid–deep crust at ~20–16 Ma, best documented in the Yazgulom, Sarez, and Muskol-Shatput domes. 5) Input of asthenosphere heat into the Pamir lithosphere caused magmatism and prolonged high-grade metamorphism and migmatization best observed in the Shakhdara dome, Taxkorgan complex, Dunkeldik volcanic field, and likely the Hindu Kush and Karakoram (Mahéo et al., 2002). 6) Thermal weakening of the Pamir crust and the delaminating Asian lithosphere, which by then was telescoped northward by the indenting Indian lithospheric mantle (Mechie et al., 2012; Sippl et al., 2013b), continued to drive collapse of the Pamir Plateau via crustal extension in the Shakhdara (Stübner et al., 2013a) and the Muztagata-Kongur Shan domes (Robinson et al., 2004, 2007) into the lowland of the Tajik basin (Stübner et al., 2013a). Roughly ≤90 km mid-deep crustal extension in the Shakhdara dome have been active from ~15-7 Ma (this study) and low-temperature thermochronometers extend this to ~4-2 Ma (Stübner et al., 2013b) (Fig. 22A). A maximum of ≤35 km extension in the Muztagata-Kongur Shan dome started at ~8-7 Ma and is active (Robinson et al., 2007). Active, north-northeast trending, sinistral transtensional fault systems—dissecting the Pamir's interior— trace active collapse (Schurr et al., 2014).

Conclusions

The switch to exhumation of the Pamir gneiss domes is recorded by U-Pb titanite dates and Zr-in-titanite thermometry from igneous intrusions, prograde titanite, and retrograde titanite. The early stages of exhumation in the Central and South Pamir domes began synchronously around ~20 Ma, but ended asynchronously. The Central Pamir domes cooled more rapidly by ~16 Ma, whereas the South Pamir were hotter than 650 ºC until ~10 Ma. Age–elevation profiles from the South Pamir indicate that the northern Gunt shear zone began cooling ~21

Ma, whereas the core of the dome and the South Pamir shear zone began cooling ~14 Ma. The initiation of exhumation in both the Central and South Pamir may have been driven by breakoff of the India lithosphere at ~20 Ma, followed until 10 Ma by slower exhumation of the South Pamir driven in part by the ongoing subduction of the Asian lithosphere.

References

Aleinikoff, J.N., Wintsch, R.P., Tollo, R.P., Unruh, D.M., Fanning, C.M., and Schmitz,

M.D., 2007, Ages and origins of rocks of the Killington dome, south-central Conneticut:

Implications for the tectonic evolution of southern New England: American Journal of

Science, vol. 307, p. 63–118, doi: 10.2475/01.2007.04.

Aleinikoff, J. N., Wintsch, R. P., Fanning, C. M., and Dorais, M. J., 2002, U–Pb

geochronology of zircon and polygenetic titanite from the Glastonbury Complex,

Connecticut, USA: an integrated SEM, EMPA, TIMS, and SHRIMP study: Chemical

Geology, vol. 188(1), p. 125-147.

Andersen, T., 2002, Correction of common lead in U-Pb analyses that do not report 204Pb:

Chemical Geology, vol. 192, p. 59–79.

Argles, T. W., & Edwards, M. A., 2002, First evidence for high-grade, Himalayan-age

synconvergent extension recognized within the western syntaxis—Nanga Parbat,

Pakistan: Journal of structural geology, vol. 24(8), p. 1327-1344.

Bachmann, O., Dungan, M.A., and Bussy, F., 2005, Insights into shallow magmatic

processes in large silicic magma bodies: the trace element record in the Fish Canyon

magma body, Colorado: Contributions to Mineralogy and Petrology, vol. 149, p. 338–

349.

Beaumont, C., Jamieson, R. A., Nguyen, M. H., & Lee, B., 2001, Himalayan tectonics

explained by extrusion of a low-viscosity crustal channel coupled to focused surface

denudation: Nature, vol. 414(6865), p. 738-742.

Berman, R. G., 1988, Internally-consistent thermodynamic data for minerals in the system

Na2O-K2O-CaO-MgO-FeO-Fe2O3-Al2O3-SiO2-TiO2-H2O-CO2: Journal of Petrology,

vol. 29(2), p. 445-522.

Bershaw, J., Garzione, C.N., Schoenbohm, L., Gehrels, G., and Tao, L., 2012, Cenozoic evolution of the Pamir plateau based on stratigraphy, zircon provenance, and stable isotopes of foreland basin sediments at Oytag (Wuyitake) in the Tarim Basin (west China): Journal of Asian Earth Sciences, vol. 44, p. 136–148.

Bingen, B., Demaiffe, D., and Hertogen, J., 1996, Redistribution of rare earth elements, thorium, and uranium over accessory minerals in the course of amphibolite to granulite facies metamorphism: The role of apatite and monazite in orthogneisses from southwestern Norway: Geochimica et Cosmochimica Acta, v. 60, p. 1341–1354, doi:10.1016/0016-7037(96)00006-3.

Bonimici, C.E., Kozdon, R., Ushikubo, T., and Valley, J.W., 2014, Intragrain oxygen isotope zoning in titanite by SIMS: Cooling rates and fluid infiltration along the Carthage-Colton Mylonite Zone, Adirondack Mountains, NY, USA: Journal of Metamorphic Geology, vol. 32, p. 71–92. doi: 10.1111/jmg.12059.

Bonamici, C.E., Kozdon, R., Ushikubo, T., and Valley, J.W., 2011, High-resolution P-T-t paths from $\partial^{18}O$ zoning in titanite: A snapshot of late-orogenic collapse in the Grenville of New York: Geology, vol. 39, p. 969–962.

Brunel, M., Arnaud, N., Tapponnier, P., Pan, Y., and Wang, Y., 1994, Kongur Shan normal fault: Type example of mountain building assisted by extension (Karakoram fault, easter Pamir: Geology, vol. 22, p. 707–710, doi: 10.1130/0091-7613(1994)022<0707:KSNFTE>2.2.CO;2.

Burtman, V.S. and Molnar, P.H. ,1993, Geological and geophysical evidence for deep subduction of continental crust beneath the Pamir: Geological Society of America Specail Papers, vol. 281, p. 1–76, doi: 10.1130/SPE281-p1.

Cao, K., Bernet, M., Wang, G.C., van der Beek, P., Wang, A., Zhang, K.X., and Enkelmann, E., 2013, Focused Pliocene–Quaternary exhumation of the Eastern Pamir domes, western China: Earth and Planetary Science Letters, vol. 363, p. 16–26, doi: 10.1016/j.epsl.2012.12.023.

Chemenda, A.I., Mattauer, M., Malavieille, J., and Bokun, A.N. ,1995, A mechanism for syn-collisional rock exhumation and associated normal faulting: Results from physical modelling: Earth and Planetary Science Letters, vol. 132(1), p. 225-232.

Chen, W.P., Martin, M., Tseng, T.L., Nowack, R.L., Hung, S.H., and Huang, S., 2010, Shear-wave birefringence and current configuration of converging lithosphere under Tibet: Earth and Planetary Science Letters, v. 295, p. 297–304, doi:10.1016/j.epsl.2010.04.017.

Cherniak, D.J., 1993, Lead diffusion in titanite and preliminary results on the effects of radiation damage on Pb transport. Chemical Geology, vol. 110(1), p. 177-194.

Cherniak, D.J., 2006, Zr diffusion in titanite: Contributions to Mineralogy and Petrology, vol. 152(5), p. 639-647.

Cherniak, D.J., 2010, Diffusion in accessory minerals: zircon, titanite, apatite, monazite and xenotime: Reviews in Mineralogy and Geochemistry, vol. 72(1), p. 827-869.

Cherniak, D.J., Watson, E.B., Grove, M., and Harrison, T.M., 2004, Pb diffusion in monazite: A combined RBS/SIMS study: Geochimica et Cosmochimica Acta, v. 68, p. 829–840, doi:10.1016/j.gca.2003.07.012.

Chung, S.L., Chu, M.F., Zhang, Y., Xie, Y., Lo, C.H., Lee, T.Y., Lan, C.Y., Li, X., Zhang, Q., and Wang, Y., 2005, Tibetan tectonic evolution inferred from spatial and temporal variations in post-collisional magmatism: Earth-Science Reviews, v. 68, p. 173–196, doi:10.1016/j.earscirev.2004.05.001.

Chung, S.L., Liu, D., Ji, J., Chu, M.F., Lee, H.Y., Wen, D.J., Lo, C.H., Lee, T.Y., Qian, Q., and Zhang, Q., 2003, Adakites from continental collision zones: Melting of thickened lower crust beneath southern Tibet: Geology, v. 31, p. 1021–1024, doi:10.1130/G19796.1.

Corfu, F., 1996, Multistage zircon and titanite growth and inheritance in an Archean gneiss complex, Winnipeg River Subprovince, Ontario: Earth and Planetary Science Letters, vol. 141(1), p. 175-186.

Corrie, M.J. and Kohn, S.L., 2011, Preserved Zr-temperatures and U-Pb ages in high-grade metamorphic titanite: Evidence for a static hot channel in the Himalayan orogen: Earth and Planetary Sciences, vol. 311, p. 136–143, doi: 10.1016/j.epsl.2011.09.008.

Costa, F., Chakraborty, S., and Dohmen, R., 2003, Diffusion coupling between trace and major elements and a model for calculation of magma residence times using plagioclase: Geochica et Cosmochimica Acta, vol. 67, p. 2189–2200, doi: 10.1016/S0016-7073(02)01345-5.

Costa, F. and Dungan, M., 2005, Short time scales of magmatic assimilation from diffusion modeling of multiple elements in olivine: Geology, vol. 33, p. 837–840, doi: 10.1130/G21675.1.

Cottle, J.M., Kylander-Clark, A.R., Vrijmoed, J.C., 2012, U-Th/Pb geochronology of detrital zircon and monazite by single shot laser ablation inductively coupled plasma mass spectrometry (SS-LA-ICPMS): Chemical Geology, vol. 332–333, p. 136–147, doi: 10.016/j.chemgeo.2012.09.035.

Cottle, J.M., Searle, M.P., Horstwood, M.S.A., and Waters, D.J., 2009, Timing of midcrustal metamorphism, melting, and deformation in the Mount Everest region of southern Tibet

revealed by U(-Th)-Pb geochronology: The Journal of Geology, v. 117, p. 643–664, doi:10.1086/605994.

DeCelles, P., Kapp, P., Quade, J., and Gehrels, G.E., 2011, Oligocene-Miocene Kailas basin, southwestern Tibet: Record of postcollisional upper-plate extension in the Indus-Yarlung suture zone: Geological Society of America Bulletin, v. 123, p. 1337–1362, doi:10.1130/B30258.1.

Dodson, M.H., 1973, Closure temperature in cooling geochronological and petrological systems: Contributions to Mineralogy and Petrology, vol. 40, p. 259–274.

Ducea, M.N., Lutkov, V., Minaev, V.T., Hacker, B., Ratschbacher, L., Luffi, P., Schwab, M., Gehrels, G.E., McWilliams, M., Vervoort, J., and Metcalf, J., 2003, Building the Pamirs: The view from the underside: Geology, vol. 31(10), p. 849-852.

England, P. and Molnar, P., 1990, Surface uplift, uplift of rocks, and exhumation of rocks: Geology, vol. 18(12), p. 1173-1177.

England, P., and Houseman, G., 1989, Extension during continental convergence, with application to the Tibetan Plateau: Journal of Geophysical Research, v. 94, p. 17561–17579, doi:10.1029/JB094iB12p17561.

England, P.C., and Thompson, A.B., 1984, Pressure-temperature-time paths of regional metamorphism I. Heat transfer during the evolution of regions of thickened continental crust: Journal of Petrology, v. 25, p. 894–928, doi:10.1093/petrology/25.4.894.

Forsyth, D., and Uyeda, S., 1975, On the relative importance of the driving forces of plate motion: Geophysical Journal of the Royal Astronomical Society, v. 43, p. 163–200, doi:10.1111/j.1365-246X.1975.tb00631.x.

Foster, G., Kinney, P., Vance, D., Prince, C., and Harris, N., 2000, The significance of monazite U-Th-Pb age data in metamorphic assemblages; a combined study of monazite

and garnet chronometry: Earth and Planetary Science Letters, v. 181, p. 327–340, doi:10.1016/S0012-821X(00)00212-0.

Foster, G., Parrish, R.R., Horstwood, M.S.A., Cheney, S., Pyle, J., and Gibson, H.D., 2004, The generation of prograde P-T-t points and paths; a textural, compositional, and chronological study of metamorphic monazite: Earth and Planetary Science Letters, v. 228, p. 125–142, doi:10.1016/j.epsl.2004.09.024.

Frost, B.R., Chamberlain, K.R., and Schumacher, J.C., 2001, Sphene (titanite): phase relations and role as a geochronometer: Chemical Geology, vol. 172(1), p. 131-148.

Frost, C.D. and Fanning, C.M., 2006, Archean geochronological framework of the Bighorn Mountains, Wyoming: Canadian Journal of Earth Sciences, vol. 43(10), p. 1399-1418.

Gao, S., Liu, X., Yuan, H., Hattendorf, B., Günther, D., Chen, L., and Hu, S., 2007, Determination of Forty Two Major and Trace Elements in USGS and NIST SRM Glasses by Laser Ablation-Inductively Coupled Plasma-Mass Spectrometry: The Journal of Geostandards and Geoanalysis, vol. 26, p. 181–196.

García, F.D., Arenas, R., Catalán, J.R.M., del Tánago, J.G., & Dunning, G.R., 1999, Tectonic evolution of the Careón ophiolite (Northwest Spain): a remnant of oceanic lithosphere in the Variscan belt: The Journal of Geology, vol. 107(5), p. 587-605.

Göğüş, O.H. and Pysklywec, R.N., 2008, Mantle lithosphere delamination driving plateau uplift and synconvergent extension in eastern Anatolia: Geology, vol. 36(9), p. 723-726.

Grew, E.S., Pertsev, N.N., Yates, M.G., Christy, A.G., Marquez, N., and Chernosky, J.V., 1994, Sapphirine + forsterite and sapphirine + humite-group minerals in an ultra-magnesian lens from Kuhi-lal, SW Pamirs, Tajikistan: Are the assemblages forbidden?: Journal of Petrology, v. 35, p. 1275–1293, doi:10.1093/petrology/35.5.1275.

Grove, M. and Harrison, T.M., 1999, Monazite Th-Pb age depth profiling: Geology, vol. 27, p. 487–490, doi: 10.1130/0091-7613(1999)027<0487:MTPADP>2.2.CO.2.

Hayden, L.A., Watson, E.B., and Wark, D.A., 2008, A thermobarometer for sphene (titanite): Contributions to Mineralogy and Petrology, vol. 155(4), p. 529-540.

Heinrich, C.A., Pettke, T., Halter, W.E., Aigner-Torres, M., Audétat, A., Günther, D., Hattendorf, B., Bleiner, D., Guillong, M., and Horn, I., 2003, Quantitative multi-element analysis of minerals, fluid and melt inclusions by laser-ablation inductively-coupled-plasma mass-spectrometry: Geochimica et Cosmochimica Acta, vol. 67, p. 3473-3497.

Hermann, J., and Rubatto, D., 2003, Relating zircon and monazite domains to garnet growth zones: Age and duration of granulite facies metamorphism in the Val Malenco lower crust: Journal of Metamorphic Petrology, v. 21, p. 833–852, doi:10.1046/j.1525-1314.2003.00484.x.

Kohn, M.J., and Malloy, M.A., 2004, Formation of monazite via prograde metamorphic reactions among common silicates: Implications for age determinations: Geochimica et Cosmochimica Acta, v. 68, p. 101–113, doi:10.1016/S0016-7037(03)00258-8.

Kohn, M.J., and Parkinson, C.D., 2002, Petrologic case for Eocene slab breakoff during the Indo-Asian collision: Geology, v. 30, p. 591–594, doi:10.1130/0091-7613(2002)030<0591:PCFESB>2.0.CO;2.

Kylander-Clark, A.R.C., Hacker, B.R., and Mattinson, J.M., 2008, Slow exhumation of UHP terranes: Titanite and rutile ages of the Western Gneiss Region, Norway: Earth and Planetary Science Letters, vol. 272, p. 531–540, doi: 10.1016/j.epsl.2008.05.019.

Kylander-Clark, A.R.C., Hacker, B.R., and Cottle, J.M., 2013, Laser-ablation split-stream ICP petrochronology: Chemical Geology, vol. 345, p. 99–112, doi: 10.1016/j.chemgeo.2013.02.019.

Lee, J.K.W., Williams, I.S., and Ellis, D.J., 1997, Pb, U, and Th diffusion in natural zircon: Nature, vol. 390, p. 159–162, doi: 10.1038/36554.

Lee, J., and Whitehouse, M.J., 2007, Onset of mid-crustal extensional flow in southern Tibet: Evidence from U/Pb zircon ages: Geology, v. 35, p. 45–48, doi:10.1130/G22842A.1.

Lee, J., Hacker, B.R., and Wang, Y., 2004, Evolution of the north Himalayan Gneiss Domes: Structure and metamorphic studies in Mabja Dome, southern Tibet: Journal of Structural Geology, v. 26, p. 2297–2316, doi:10.1016/j.jsg.2004.02.013.

Lee, J., Hacker, B.R., Dinklage, W.S., Gans, P.B., Calvert, A., Wang, Y., and Chen, W., 2000, Evolution of the Kangmar Dome, southern Tibet: Structural, petrologic, and thermochronologic constraints: Tectonics, v. 19, p. 872–895, doi:10.1029/1999TC001147.

Liou, J.G., 1974, Mineralogy and chemistry of glassy basalts, Coastal Range ophiolites, Taiwan: Geological Society of America Bulletin, vol. 85(1), p. 1-10.

Mazdab, F.K., 2009, Characterization of flux-grown trace-element-doped titanite using the high-mass-resolution ion microprobe (SHRIMP–RG): The Canadian Mineralogist, vol. 47(4), p. 813-831.

Molnar, P. and Lyon-Caen, H., 1988, Some simple physical aspects of the support, structure, and evolution of mountain belts: Geological Society of America Special Papers, vol. 218, p. 179–208, doi: 10.1130/SPE218-p179.

Nábělek, J., Hetenyi, G., Vergne, J., Sapkota, S., Kafle, B., Jiang, M., Su., H., Chen, J., Huang, B.S., and Hi-CLIMB Team, 2009, Underplating in the Himalaya-Tibet collision zone revealed by the Hi-CLIMB experiment: Nature, v. 325, p. 1371–1374.

Negredo, A.M., Replumaz, A., Villaseñor, A., and Guillot, S., 2007, Modeling the evolution of continental subduction processes in the Pamir-Hindu Kush region: Earth and Planetary Science Letters, v. 259, p. 212–225, doi:10.1016/j.epsl.2007.04.043.

Nelson, K.D., and 26 others, 1996, Partially molten middle crust beneath southern Tibet: synthesis of project INDEPTH results: Science, v. 274, p. 1684–1688, doi:10.1126/science.274.5293.1684.

Nikolaev, V.G., 2002, Afghan-Tajik depression: Architecture of sedimentary cover and evolution: Russian Journal of Earth Sciences, vol. 4 (6), p. 399-421.

Paquette, J.L., Goncalves, P., Devouard, B., and Nicollet, C., 2004, Micro-drilling ID-TIMS U-Pb dating of single monazites: A new method to unravel complex poly-metamorphic evolutions. Applications to the UHT granulites of Andriamena (North-Central Madagascar): Contributions to Mineralogy and Petrology, vol. 147, p. 110–122.

Parrish, R.R., Gough, S.J., Searle, M.P., and Waters, D.J., 2006, Plate velocity exhumation of ultrahigh-pressure eclogites in the Pakistan Himalaya: Geology, vol. 34, p. 989–992, doi: 10.1130/G22796A.1.

Paul, J., Bürgmann, R., Gaur, V.K., Bilham, R., Larson, K.M., Ananda, M.B., Jade, S., Mukal, M., Anupama, T.S., Satyal, G., and Kumar, D., 2001, The motion and active deformation of India: Geophysical Research Letters, vol. 28(4), p. 647-650.

Prowatke, S. and Klemme, S., 2005, Effect of melt composition on the partitioning of trace elements between titanite and silicate melt: Geochimica et Cosmochimica Acta, vol. 69, p. 695–709, doi: 10.1016/j.gca.2004.06.037.

Quigley, M., Liangjun, Y., Wilson, C.J.L., Sandiford, M., and Phillips, D., 2006, 40Ar/39Ar thermochronology of the Kampa Dome, southern Tibet: Implications for tectonic

evolution of the north Himalayan gneiss domes: Tectonophysics, v. 421, p. 269–297, doi:10.1016/j.tecto.2006.05.002.

Replumaz, A., Guillot, S., Villaseñor, A., & Negredo, A. M., 2012, Amount of Asian lithospheric mantle subducted during the India/Asia collision. Gondwana Research.

Replumaz, A., Negredo, A.M., Guillot, S., and Villaseñor, A., 2010, Multiple episodes of continental subduction during India/Asia convergence: Insight from seismic tomography and tectonic reconstruction: Tectonophysics, v. 483, p. 125–134, doi:10.1016/j.tecto.2009.10.007.

Rey, P., Vanderhaeghe, O., and Teyssier, C., 2001, Gravitational collapse of the continental crust: definition, regimes and modes: Tectonophysics, vol. 342(3), p. 435-449.

Robinson, A.C., Ducea, M., and Lapen, T.J., 2012, Detrital zircon and isotopic constraints on the crustal architecture and tectonic evolution of the northeastern Pamir: Tectonics, vol. 31(2), TC2016, doi: 10.1029/2011TC003013.

Rubatto, D. and Hermann, J., 2001, Exhumation as fast as subduction?: Geology, vol. 29, p. 3-6, doi: 10.1130/0091-7613(2001)029<0003:EAFAS>2.0.CO;2.

Rutte, D., Stearns, M., and Ratschbacher, L., 2013, The eastern Central Pamir Gneiss Domes: temporal and spatial geometry of burial and exhumation: EGU General Assembly Conference Abstracts, vol. 15, p. 6090.

Schaltegger, U., Brack, P., Ovtcharova, M., Peytcheva, I., Schoene, B., Stracke, A., and Bargossi, G.M., 2009, Zircon and titanite recording 1.5 million years of magma accretion, crystallization and initial cooling in a composite pluton (southern Adamello batholith, northern Italy): Earth and Planetary Science Letters, vol. 286, p. 208–216, doi: 10.1016/j.epsl.2009.06.028.

Schmidt, J., Hacker, B.R., Ratschbacher, L., Stübner, K., Stearns, M., Kylander-Clark, A., Cottle, J.M., Alexander, A., Webb, G., Gehrels, G., and Minaev, V., 2011, Cenozoic deep crust in the Pamir: Earth and Planetary Science Letters, vol. 312, p. 411–421, doi: 10.1 016/j.eps1.2011.1 0.034.

Schmitz, M.D. and Bowring, S.A., 2001, U-Pb zircon and titanite systematics of the Fish Canyon Tuff: an assessment of high-precision U-Pb geochronology and its application to young volcanic rocks: Geochimica et Cosmochimica Acta, vol. 65, p. 2571–2587, doi: 10.1016/S0016-7037(01)00616-0.

Schoenbohm, L.M., Burchfiel, B.C., and Liangzhong, C., 2006, Propagation of surface uplift, lower crustal flow, and Cenozoic tectonics of the southeast margin of the Tibetan Plateau: Geology, vol. 34(10), p. 813-816.

Schoene, B., Crowley, J.L., Condon, D.J., Schmitz, M.D., and Bowring, S.A., 2006, Reassessing the uranium decay constants for geochronology using ID-TIMS U-Pb data: Geochimica et Cosmochimica Acta, vol. 70, p. 426–445.

Schurr, B., Ratschbacher, L., Sippl, C., Gloaguen, R., Yuan, X., and Mechie, J., in press, Seismotectonics of the Pamir, central Asia: Tectonics.

Schwab, G., Katzung, G., Ludwig, A.O., Lützner, H., 1980. Neogene Molasse-Sedimentation in der Tadschikischen Depression (tadschikische SSR). Zeitschrift für Angewandte.Geologie, vol. 26/5, p. 225–238.

Schwab, M., Ratschbacher, L., Siebel, W., McWilliams, M., Minaev, V., Lutkov, V., Chen, F., Stanek, K., Nelson, B., Frisch, W., and Wooden, J.L., 2004, Assembly of the Pamirs: Age and origin of magmatic belts from the southern Tien Shan to the southern Pamirs and their relation to Tibet: Tectonics, vol. 23, TC4002, doi:10.1029/2003TC001583.

Scott, D.J. and St-Onge, M.R., 1995, Constraints on Pb closure temperature in titanite based on rocks from the Ungava orogen, Canada: Implications for U-Pb geochronology and PTt path determinations: Geology, vol. 23(12), p. 1123-1126.

Selverstone, J., 2004, Are the Alps Collapsing?: Annual Review of Earth and Planetary Sciences, vol. 33, p. 113–132, doi: 10.1146/annurev.earth.33.092203.122535

Shannon, R.D., 1976, Revised effective ionic radii and systematic studies of interatomic distances in halides and chalcogenides: Acta Crystallographica, vol. A32, p. 751–767.

Simpson, R.L., Parrish, R.R., Searle, M.P., and Waters, D.J., 2000, Two episodes of monazite crystallization during metamorphism and crustal melting in the Everest region of the Nepalese Himalaya: Geology, vol. 28, p. 403–406, doi:10.1130/0091-7613(2000)28<403:TEOMCD>2.0.CO;2.

Sippl, C., Schurr, B., Tympel, J., Angiboust, S., Mechie, J., Yuan, X., Schneider, F.M., Sobolev, S.V., Ratschbacher, L., and Haberland, C., 2013, Deep burial of Asian continental crust beneath the Pamir imaged with local earthquake tomography: Earth and Planetary Science Letters, vol. 384, p. 165-177, doi: 10.1016/j.epsl.2013.10.013.

Sippl, C., Schurr, B., Yuan, X., Mechie, J., Schneider, F.M., Gadoev, M., Orunbaev, S., Oimahmadov, I., Haberland, C., Abdybachaev, U., Minaev, V., Negmatullaev, S., and Radjabov, N., 2013, Geometry of the Pamir-Hindu Kush intermediate-depth earthquake zone from local seismic data: Journal of Geophysical Research: Solid Earth, vol. 118, p. 1438–1457, doi. 10.1002/jgrb.50128.

Söderlund, U., Jarl, L.G., Persson, P.O., Stephens, M.B., and Wahlgren, C.H., 1999, Protolith ages and timing of deformation in the eastern, marginal part of the Sveconorwegian orogen, southwestern Sweden: Precambrian Research, vol. 94(1), p. 29-48.

Spear, F.S., 1981, Amphibole-plagioclase equiibria: An empirical model for the relation albite+tremolite=edenite+4 quartz: Contributions to Mineralogy and Petrology, vol. 77, p. 355–364.

Spencer, K. J., Hacker, B.R., Kylander-Clark, A.R.C., Andersen, T.B., Cottle, J.M., Stearns, M.A., Poletti, J.E., and Seward, G.G.E., 2013, Campaign-style titanite U-Pb dating by laser-ablation ICP: Implications for crustal flow, phase transformations and titanite closure: Chemical Geology, vol. 341, p. 84–101, doi: 10.1016/j.chemgeo.2012.11.012.

Stacey, J.S. and Kramers, J.D., 1975, Approximation of terrestrial lead isotope evolution by a two-stage model: Earth and Planetary Science Letters, vol. 26, p. 207–221, doi: 10.1016/0012-0821X(75)90088-6.

Stearns, M.A., Hacker, B.R., Ratschbacher, L., Lee, J., Cottle, J.M., and Kylander-Clark, A.R.C., 2013, Synchronous Oligocene–Miocene metamorphism of the Pamir and the north Himalaya driven by plate-scale dynamics: Geology, vol. 41(10), p. 1071-1074.

Streule, M.J., Searle, M.P., Waters, D.J., and Horstwood, M.S.A., 2010, Metamorphism, melting, and channel flow in the Greater Himalayan Sequence and Makalu leucogranites: Constraints form thermobarometry, metamorphic modeling, and U-Pb geochronology: Tectonics, v. 29, TC5011, doi:10.1029/2009TC002533.

Stübner, K., Ratschbacher, L., Rutte, D., Stanek, K., Minaev, V., Wiesinger, M., and Gloaguen, R., 2013a, The giant Shakhdara migmatitic gneiss dome, Pamir, India-Asia collision zone: 1. Geometry and kinematics: Tectonics, vol. 32(4), p. 948-979.

Stübner, K., Ratschbacher, L., Weise, C., Chow, J., Hofmann, J., Khan, J., Rutte, D., Sperner, B., Pfänder, J.A., Hacker, B.R., Dunkl, I., Tichomirowa, M., Stearns, M. A., and Project TIPAGE members, 2013b, The giant Shakhdara migmatitic gneiss dome, Pamir,

India-Asia collision zone: 2. Timing of dome formation: Tectonics, vol. 32(5), p. 1404-1431, doi: 10.1002/tect.20059.

Thiede, R.C., Sobel, E.R., Chen, J.C., Schoenbohm, E.R., Stockli, D.F., Sudo, M., and Strecker, M.R., Late Cenozoic extension and crustal doming in the India-Eurasia collision zone: New thermochronologic constraints from the NE Chinese Pamir: Tectonics, vol. 32, p. 763–779, doi: 10.1002/tect.20050.

Torvela, T. and Ehlers, C., 2010, From ductile to brittle deformation: structural development and strain distribution along a crustal-scale shear zone in SW Finland: International Journal of Earth Sciences, vol. 99, p. 1133–1152.

Troitzsch, U. and Ellis, D.J., 2002, Thermodynamic properties and stability of AlF-bearing titanite CaTiOSiO4–CaAlFSiO4: Contributions to Mineralogy and Petrology, vol. 142(5), p. 543-563.

van Hinsbergen, D.J.J., Steinberger, B., Doubrovine, P.V., and Gassmöller, R., 2011, Acceleration and deceleration of India-Asia convergence since the Cretaceous: Roles of mantle plumes and continental collision: Journal of Geophysical Research, v. 116, B06101, doi:10.1029/2010JB008051.

Vance, D., and Mahar, E., 1998, Pressure-temperature paths form $P-T$ pseudosections and zoned garnets: Potential, limitations and examples from the Zanskar Himalaya, NW India: Contributions to Mineralogy and Petrology, v. 132, p. 225–245, doi:10.1007/s004100050419.

Vermeesch, P., 2012, On the visualisation of detrital age distributions: Chemical Geology, vol. 312, p. 190-194.

Watson, E.B. and Cherniak, D.J., 2013, Simple equations for diffusion in response to heating: Chemical Geology, vol. 335, p. 93–104, doi: 10.1016/j.chemgeo.2012.10.054.

Williams, M.L., Jercinovic, M.J., and Terry, M.P., 1999, Age mapping and dating of monazite on the electron microprobe: Deconvoluting multistage tectonic histories: Geology, v. 27, p. 1023–1026, doi:10.1130/0091-7613(1999)027<1023:AMADOM>2.3.CO;2.

Williams, M.L., Jercinovic, M.J., Harlov, D.E., Budzyń, B., and Hetherington, C.J., 2011, Resetting monazite ages during fluid-related alteration: Chemical Geology, v. 283, p. 218–225, doi:10.1016/j.chemgeo.2011.01.019.

Yin, A. and Harrison, T.M., 2000, Geologic evolution of the Himalayan-Tibetan orogen: Annual Review of Earth and Planetary Sciences, vol. 28(1), p. 211-280.

York, D., 1966, Least-squares fitting of a straight line: Canadian Journal of Physics, vol. 44, p. 1079–1086, doi: 10.1139/p66-090.

Yuan, H.L., Gao, S., Dai, M.N., Zong, C.L., Günther, D., Fontaine, G.H., Liu, X.M., and Diwu, C.R., 2008, Simultaneous determinations of U-Pb age, Hf isotopes and trace element compositions of zircon by excimer laser-ablation quadrupole and multiple-collector ICP-MS: Chemical Geology, v. 247, p. 100–118, doi:10.1016/j.chemgeo.2007.10.003.

Zhang, L.S. and Schärer, U., 1996, Inherited Pb components in magmatic titanite and their consequence for the interpretation of U-Pb ages: Earth and Planetary Science Letters, vol. 138, p. 57–65, doi: 10.1016/0012-821X(95)00237-7.

Appendices:

Appendix 1 - Chapter 1, Excel® file containing titanite U/Th-Pb ratios and trace-element

concentrations from single-shot laser-ablation split stream ICP-MS

Appendix 2 - Chapter 2, Adobe® PDF of tectonic event and Pamir geochronology summary,

monazite U/Th-Pb and REE diagrams, U/Th-Pb ratios and trace-element concentrations

from laser-ablation split stream (LASS) ICP-MS, monazite X-ray element maps

Appendix 3 - Chapter 3, Excel® file containing titanite U/Th-Pb data

Appendix 4 - Chapter 3, Excel® file containing titanite Zr and apparent temperatures